Title

Structural Basis for Shelterin Bridge Assembly

Journal

Molecular Cell, 68(4)

ISSN

1097-2765

Authors

Kim, Jin-Kwang

Liu, Jinqiang

Hu, Xichan

et al.

Publication Date

2017-11-01

DOI

10.1016/j.molcel.2017.10.032

Peer reviewed

Article

Molecular Cell

Structural Basis for Shelterin Bridge Assembly

Graphical Abstract

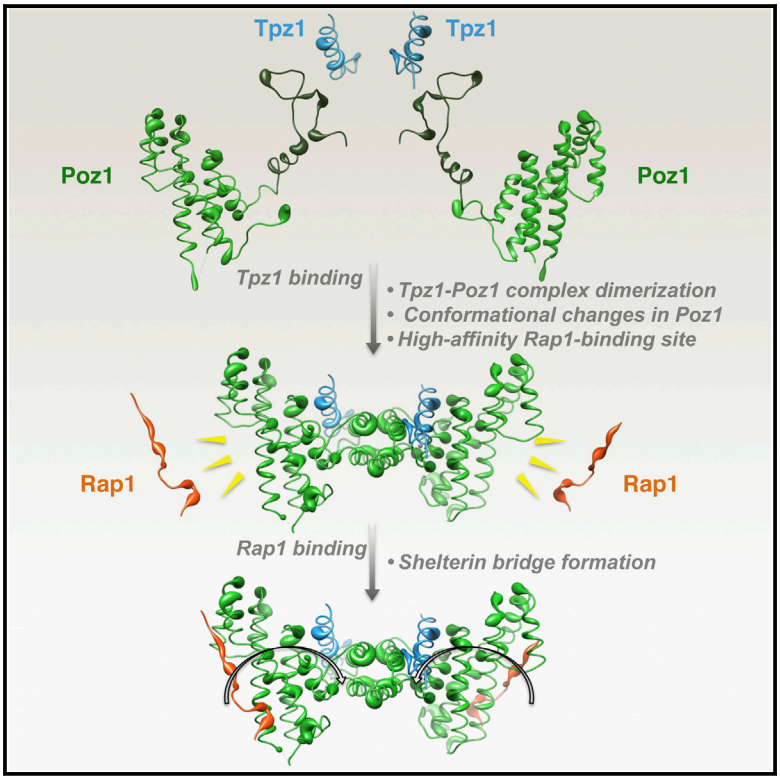

Authors

Jin-Kwang Kim, Jinqiang Liu, Xichan Hu, ..., Lan Huang, Elizabeth A. Komives, Feng Qiao

Correspondence

qiao@uci.edu

In Brief

Shelterin complex protects chromosome ends and regulates telomere elongation. Kim et al. solved the crystal structure of the fission yeast shelterin bridge Tpz1-Poz1-Rap1 complex and revealed its assembly mechanism at the atomic level, uncovering cooperativity as a conserved driving force for shelterin bridge assembly.

Highlights

- The structure of shelterin bridge Tpz1-Poz1-Rap1 complex solved at 2.3 Å resolution
- The shelterin bridge assembly is a cooperative process
- Perturbation of the cooperative assembly leads to dysfunctional telomere regulation
- Cooperativity is a conserved driving force for human shelterin bridge assembly

Kim et al., 2017, Molecular Cell *68*, 698–714
November 16, 2017
https://doi.org/10.1016/j.molcel.2017.10.032

CellPress

CellPress

Molecular Cell
Article

Structural Basis for Shelterin Bridge Assembly

Jin-Kwang Kim,[1,6] Jinqiang Liu,[1,6] Xichan Hu,[1] Clinton Yu,[2] Kyle Roskamp,[3] Banumathi Sankaran,[4] Lan Huang,[2] Elizabeth A. Komives,[5] and Feng Qiao[1,7,*]

[1]Department of Biological Chemistry, School of Medicine, University of California, Irvine, Irvine, CA 92697-1700, USA
[2]Department of Physiology and Biophysics, School of Medicine, University of California, Irvine, Irvine, CA 92697-4560, USA
[3]Department of Chemistry, University of California, Irvine, Irvine, CA 92697-2025, USA
[4]Berkeley Center for Structural Biology, Physical Biosciences Division, Lawrence Berkeley Laboratory, Berkeley, CA 94720, USA
[5]Department of Chemistry and Biochemistry, University of California, San Diego, La Jolla, CA 92093-0378, USA
[6]These authors contributed equally
[7]Lead Contact
*Correspondence: qiao@uci.edu
https://doi.org/10.1016/j.molcel.2017.10.032

SUMMARY

Telomere elongation through telomerase enables chromosome survival during cellular proliferation. The conserved multifunctional shelterin complex associates with telomeres to coordinate multiple telomere activities, including telomere elongation by telomerase. Similar to the human shelterin, fission yeast shelterin is composed of telomeric sequence-specific double- and single-stranded DNA-binding proteins, Taz1 and Pot1, respectively, bridged by Rap1, Poz1, and Tpz1. Here, we report the crystal structure of the fission yeast Tpz1$^{475-508}$-Poz1-Rap1$^{467-496}$ complex that provides the structural basis for shelterin bridge assembly. Biochemical analyses reveal that shelterin bridge assembly is a hierarchical process in which Tpz1 binding to Poz1 elicits structural changes in Poz1, allosterically promoting Rap1 binding to Poz1. Perturbation of the cooperative Tpz1-Poz1-Rap1 assembly through mutation of the "conformational trigger" in Poz1 leads to unregulated telomere lengthening. Furthermore, we find that the human shelterin counterparts TPP1-TIN2-TRF2 also assemble hierarchically, indicating cooperativity as a conserved driving force for shelterin assembly.

INTRODUCTION

Telomeres are DNA-protein complexes that protect the ends of eukaryotic chromosome from degradation and recognition as DNA damage sites (Palm and de Lange, 2008). Telomere integrity is essential for cell survival and proliferation (Ferreira et al., 2004). Dysfunctional telomeres can initiate genomic instability, cellular senescence, and organismal aging (Batista and Artandi, 2013). Telomeric DNA consists of tandem DNA repeats, which are G-rich in one strand (called the G-strand) and C-rich in the complementary stand (called the C-strand). The G-strand extends beyond the C-strand, forming a single-stranded overhang. The 3′ end of the single-stranded overhang acts as the substrate for telomerase—a reverse transcriptase (Nakamura et al., 1997) with its intrinsic RNA as the template—to extend the telomeric DNA (Autexier and Lue, 2006; Collins, 2006; Greider and Blackburn, 1985, 1987; Wu et al., 2017). Telomere shortening that is not countered by telomerase activity can directly lead to replicative senescence of cancer cells and prevent them from proliferating indefinitely. Thus, inhibiting telomere elongation, such as via telomerase inhibitors, represents a promising cancer therapeutic strategy (Baerlocher et al., 2015; Harley, 2008; Tefferi et al., 2015).

The basic structure and function of telomeres are conserved among eukaryotes (Palm and de Lange, 2008). A multi-protein complex called shelterin is vital for telomere function. Shelterin acts to regulate telomere elongation by telomerase, and to protect the ends of linear chromosomes from degradation and recognition as DNA damage sites (Artandi and Cooper, 2009; Jain and Cooper, 2010; Palm and de Lange, 2008). In human cells, the shelterin complex consists of double-stranded DNA (dsDNA) binders TRF1 and TRF2, single-stranded DNA (ssDNA) binder POT1, and RAP1, TIN2, and TPP1 (de Lange, 2005). Shelterin components connect telomeric dsDNA with ssDNA by forming a proteinaceous bridge. Specifically, telomeric dsDNA binders TRF1 and TRF2 recruit TIN2 and RAP1 to the telomere; TIN2 then recruits TPP1-POT1 complex to the telomere (Takai et al., 2011). The shelterin architecture in fission yeast, *Schizosaccharomyces pombe*, closely resembles that of mammals (Miyoshi et al., 2008). Its dsDNA binder Taz1 (homolog of hTRF1/2) (Cooper et al., 1997) and its ssDNA binder Pot1 (Baumann and Cech, 2001) are bridged via three other shelterin components, Rap1, Poz1 (hTIN2 homolog), and Tpz1 (Miyoshi et al., 2008). Ccq1, a telomerase recruiter and telomere activator, interacts directly with Tpz1 (shown in Figure 1A) (Hu et al., 2016; Jun et al., 2013; Moser et al., 2011; Webb and Zakian, 2012; Yamazaki et al., 2012).

In telomerase-positive cells, such as human embryonic stem cells (Hiyama and Hiyama, 2007), adult germline cells (Lansdorp, 2005), most cancer cells (Shay and Wright, 1996, 2010), and single-celled eukaryotes—ciliated protozoa and yeasts (Cohn and Blackburn, 1995)—telomeres are maintained at a defined species-specific range. Maintaining proper telomere length is critical for normal development and cellular function. While short

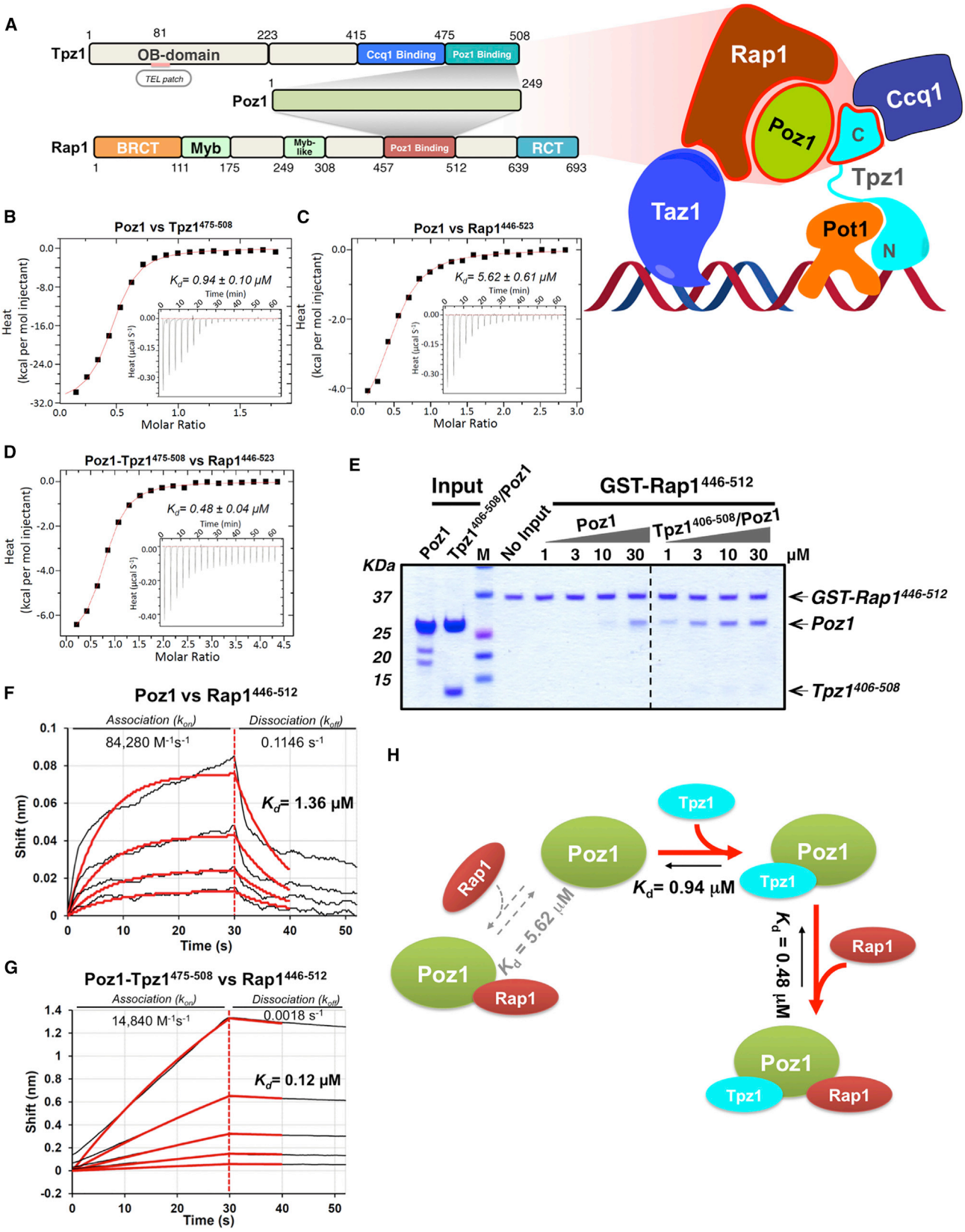

(legend on next page)

telomeres lead to defective stem cell development and differentiation, and consequently premature aging diseases, long telomeres help cells gain replicative time to accumulate other mutations (loss-of-function mutations for tumor suppressor and gain-of-function mutations for tumor activator), and thus facilitate tumorigenesis (Bernardes de Jesus and Blasco, 2013; Günes and Rudolph, 2013). Telomere length homeostasis is controlled through dynamic switching of the telomeres between two states: telomerase-extendible and -nonextendible state, depending on the telomere length (Teixeira et al., 2004). Using *S. pombe* as a model system, we recently discovered that the complete linkage within the shelterin complex, rather than the individual shelterin component per se, regulates the extendibility of telomeres by telomerase (Jun et al., 2013; Liu et al., 2015). The importance of the shelterin linkage in regulating telomere state was further emphasized by the ability of an artificial linker, instead of shelterin components, to maintain wild-type telomere length (Pan et al., 2015). Disruption of the shelterin linkage leads to unregulated telomere elongation, emphasizing the critical role of shelterin complex assembly in telomere length regulation. However, the structural basis and the mechanistic principle underlying shelterin assembly remain largely unknown (Scott et al., 2017).

In this study, we solved crystal structures at up to 2.3 Å resolution of the fission yeast Tpz1$^{475-508}$-Poz1-Rap1$^{467-496}$ complex that provide atomic-level views of the shelterin bridge assembly process. Importantly, we find that shelterin bridge assembly is a hierarchical process in which Tpz1 binding to Poz1 induces the conformational change of Poz1 through the Poz1 N-terminal helix—the "conformational trigger"—and consequently enables high-affinity binding of Rap1 to Poz1. Furthermore, perturbation of the cooperative Tpz1-Poz1-Rap1 assembly by mutating the "conformational trigger" in Poz1 leads to unregulated telomere lengthening, signifying the importance of optimal shelterin bridge assembly in telomere length regulation. Extending our findings to humans, we find that human shelterin bridge TPP1-TIN2-TRF2 also assembles in a similar hierarchical manner, indicating cooperativity as a conserved driving force for shelterin assembly to accurately regulate telomere length homeostasis.

RESULTS

Tpz1-Poz1 Interaction Promotes Poz1-Rap1 Interaction

To elucidate the assembly mechanism of the shelterin bridge Tpz1-Poz1-Rap1 complex (Figure 1A), we first broke the assembly down to elementary steps of individually characterizing Tpz1-Poz1 and Poz1-Rap1 binary interactions. To this end, we cloned, expressed, and purified Tpz1$^{475-508}$ (C-terminal Poz1-binding domain) (Jun et al., 2013), Rap1$^{446-523}$ (Poz1-binding domain) (Fujita et al., 2012), and full-length Poz1 to homogeneity. Upon obtaining recombinant Tpz1$^{475-508}$, Poz1, and Rap1$^{446-523}$, we measured the binding affinities of Tpz1$^{475-508}$-Poz1 and Poz1-Rap1$^{446-523}$ interactions by utilizing isothermal titration calorimetry (ITC). We determined the disassociation constant (K_d) of Tpz1$^{475-508}$-Poz1 interaction to be 0.94 μM and the K_d of Poz1-Rap1$^{446-523}$ interaction to be 5.62 μM (Figures 1B and 1C). Surprisingly, when we measured the binding affinity between Rap1$^{446-523}$ and Tpz1$^{475-508}$-Poz1 complex, our ITC measurement indicates that the K_d became 480 nM (Figure 1D), about 10 times stronger than that of free Poz1 to Rap1$^{446-523}$. Indeed, in an independent GST pull-down assay, we found that GST-Rap1 can bind to as low as 3 μM Tpz1-Poz1 complex efficiently, whereas 30 μM free Poz1 is required to achieve the same level of binding (Figure 1E). Therefore, the presence of Tpz1 enhanced Poz1-Rap1 interaction, indicating that Tpz1 binding to Poz1 confers positive cooperativity for the Poz1-Rap1 interaction, ensuring that the whole Tpz1-Poz1-Rap1 complex is more stable than the sum of its parts. Moreover, real-time binding kinetics analysis using bio-layer interferometry (BLI) reveals that while the association rate (k_{on}) of Rap1 binding to free Poz1 is about five times faster than that of Rap1 to Tpz1-bound Poz1, the disassociation rate (k_{off}) of Rap1 binding to Tpz1-bound Poz1 complex is approximately 60 times slower than that of Rap1 binding to free Poz1 (Figures 1F and 1G). These results indicate that Tpz1-bound Poz1 "locks" Rap1 into the stable trimeric Tpz1$^{475-508}$-Poz1-Rap1$^{446-523}$ shelterin bridge. In addition, BLI also shows similar levels of binding affinity (K_d) to the ITC measurements for Poz1-Rap1, Tpz1-bound Poz1-Rap1 (Figures 1F and 1G), and Tpz1-Poz1 interactions (Figure S1). In summary,

Figure 1. Tpz1-Poz1 Interaction Promotes Poz1-Rap1 Interaction

(A) Schematic diagram of *S. pombe* Tpz1-Poz1-Rap1 interaction (left) in the setting of overall shelterin complex on the telomere (right). Left: domain organization of shelterin bridge components Tpz1, Poz1, and Rap1. Poz1 interacts simultaneously with the C-terminal domain of Tpz1 and a middle domain of Rap1. Right: overview of *S. pombe* shelterin complex. Double-stranded telomeric DNA-binding protein Taz1 and ssDNA-binding protein Pot1 are connected by their protein interaction partners—Rap1, Poz1, and Tpz1—forming a shelterin bridge between Taz1 and Pot1. For clarity, the stoichiometry of each individual component is not indicated in the figure; only one copy of each component is shown.

(B–D) ITC measurements of interactions between Poz1 and Tpz1$^{475-508}$ (B), Poz1 and Rap$^{1446-523}$ (C), and Tpz1$^{475-508}$-Poz1 complex and Rap1$^{446-523}$ (D). The Poz1-Tpz1$^{475-508}$ interaction has ~6-fold higher binding affinity than that of the Poz1-Rap$^{1446-523}$ interaction. The binding of Tpz1$^{475-508}$ to Poz1 increases the binding affinity of Poz1-Rap1$^{446-523}$ interaction more than 10-fold. Inserts are titration data, with the dissociation constant (K_d) value ± SD calculated from the fit shown above it. All ITC experiments were repeated twice and representative results were shown.

(E) *In vitro* GST pull-down assays examining Poz1-Rap1$^{446-512}$ and Tpz1$^{406-508}$-Poz1 complex-Rap1$^{446-512}$ interactions. Tpz1$^{406-508}$ promotes strong Poz1-Rap1$^{446-512}$ interaction (right side of the dashed line). Input: 0.1 nmole Poz1 or Tpz1$^{406-508}$-Poz1 before their incubation with GST-Rap1$^{446-512}$.

(F and G) Bio-layer interferometry (BLI) sensorgrams obtained using biosensors loaded with biotin-SUMO-tagged Rap1$^{446-512}$ (Zhao et al., 2016), incubated with different concentrations of Poz1 (F) or Tpz1$^{475-508}$-Poz1 complex (G) used as analysts. Binding curves were fit globally to a 1:1 binding model to yield equilibrium dissociation constant (K_d), as well as association (k_{on}) and dissociation (k_{off}) rate constants for Poz1-Rap1$^{446-512}$ (R^2 = 0.9778) (F) or Tpz1$^{475-508}$-Poz1 complex-Rap1$^{446-512}$ (R^2 = 0.9996) (G) interactions. Tpz1$^{475-508}$-Poz1 forms very stable complex with Rap1$^{446-512}$ and dissociates from Rap1$^{446-512}$ ~60 times slower than the dissociation of free Poz1 from Rap1$^{446-512}$, based on the k_{off}. All BLI experiments were repeated twice and representative results were shown.

(H) Assembly pathway for Tpz1-Poz1-Rap1 complex. Based on binding affinity difference, Poz1 has strong preference to bind Tpz1 first, and Tpz1-Poz1 complex then interacts with Rap1 to form the ternary complex.

See Figure S1.

Table 1. Data Collection and Refinement Statistics

Data Collection	Tpz1$^{475-508}$-Poz1-Rap1$^{467-496}$	Tpz1$^{475-508}$-Poz1$^{29-249}$	Tpz1$^{475-508}$-Poz1-Rap1$^{470-494}$	Tpz1$^{475-508}$-Poz1^{3M}-Rap1$^{470-494}$
X-ray source	ALS 821	ALS 501	ALS 501	ALS 821
Wavelength (Å)	0.999996	0.977408	0.999931	0.979644
Space group	P_1	$P3_1$	$P2_12_12_1$	$P3_121$
Unit cell (a, b, c)	56.7, 82.0, 103.5	66.1, 66.1, 123.2	83.4, 95.4, 109.2	108.6, 108.6, 132.6
(α, β, γ)	90.0, 90.0, 74.0	90.0, 90.0, 120.0	90.0, 90.0, 90.0	90.0, 90.0, 120.0
Resolution (Å)	62.71-2.30 (2.42-2.30)	57.25-3.20 (3.37-3.20)	83.33-2.50 (2.64-2.50)	94.04-3.50 (3.69-3.50)
Reflections	178,361 (26,527)	52,268 (7,698)	221,705 (33,056)	150,707 (21,965)
Unique reflections	77,768 (11,346)	9,911 (1,438)	30,787 (4,415)	11,817 (1,672)
Completeness (%)	97.6 (97.2)	99.7 (99.5)	99.9 (100.0)	100.0 (100.0)
Redundancy	2.3 (2.3)	5.3 (5.4)	7.2 (7.5)	12.8 (13.1)
R_{merge}[a]	0.103 (0.434)	0.104 (0.765)	0.087 (0.660)	0.128 (0.794)
R_{meas}	0.132 (0.555)	0.116 (0.847)	0.094 (0.708)	0.146 (0.851)
R_{pim}	0.080 (0.342)	0.050 (0.361)	0.035 (0.255)	0.040 (0.232)
CC1/2	0.983 (0.726)	0.998 (0.847)	0.998 (0.912)	0.999 (0.887)
I/sigma	5.8 (2.4)	11.5 (2.6)	13.1 (2.8)	15.1 (4.2)
Wilson B factor (Å^2)	32.5	78.2	46.2	85.5
Figure of merit	–	–	0.36 (initial)/0.77 (final)	–
Refinement				
Used reflections	77,751 (5,512)	9,872 (2,310)	30,695 (2,001)	–
Reflection used for R_{free}	1,978 (126)	514 (108)	2,000 (139)	–
Resolution (Å)	62.73-2.30 (2.36-2.30)	51.92-3.20 (3.52-3.20)	45.67-2.50 (2.56-2.50)	–
R_{work}[b]	0.1996 (0.2905)	0.2664 (0.3305)	0.2093 (0.2693)	–
R_{free}[c]	0.2247 (0.3868)	0.3165 (0.4376)	0.2626 (0.3223)	–
Number of atoms	9,273	3,513	4,450	–
Number of ions	4 (Zn)	2 (Zn)	2 (Zn)	–
Protein residues	1,076	417	525	–
Waters	317	–	34	–
B-values (Å^2)	46.4	86.7	66.1	–
RMSD bonds (Å)	0.010	0.008	0.011	–
RMSD angle (^{O})	1.1	1.5	1.28	–
Ramachandran				
favored (%)	98.0	94.5	95.9	–
allowed (%)	1.8	5.5	3.7	–
disallowed (%)	0.2	0.0	0.4	–
Rotamer outliers (%)	1.0	7.5	3.6	–
Clashscore	7.24	23.41	10.48	–
PDB ID	5WE0	5WE1	5WE2	–

The numbers in parentheses are the statistics from the highest resolution shell.
[a] $R_{merge}=\sum|I-<I>|/\sum I$
[b] $R_{work}=\sum|F_{obs}-F_{calc}|/\sum F_{obs}$
[c] $R_{free}=\sum|F_{obs}-F_{calc}|/\sum F_{obs}$, where all reflections belong to a test set of 5% randomly selected data.

based on the above binding thermodynamics and kinetics results, we conclude that the Tpz1$^{475-508}$-Poz1-Rap1$^{446-523}$ complex assembles in a cooperative manner as shown in Figure 1H.

Crystal Structure of the Tpz1-Poz1-Rap1 Complex

Our finding that Tpz1-Poz1 interaction promotes the binding of Rap1 to Tpz1-bound Poz1, forming the shelterin bridge, suggested two possible mechanisms to achieve this cooperativity. First, the association of Tpz1 with Poz1 might together create a novel composite binding site for Rap1. Alternatively, binding of Tpz1 to Poz1 could induce allosteric changes that create a high-affinity Rap1-binding site. To distinguish these two possibilities and provide an atomic view of the shelterin bridge, we decided to determine the crystal structure of the Tpz1-Poz1-Rap1

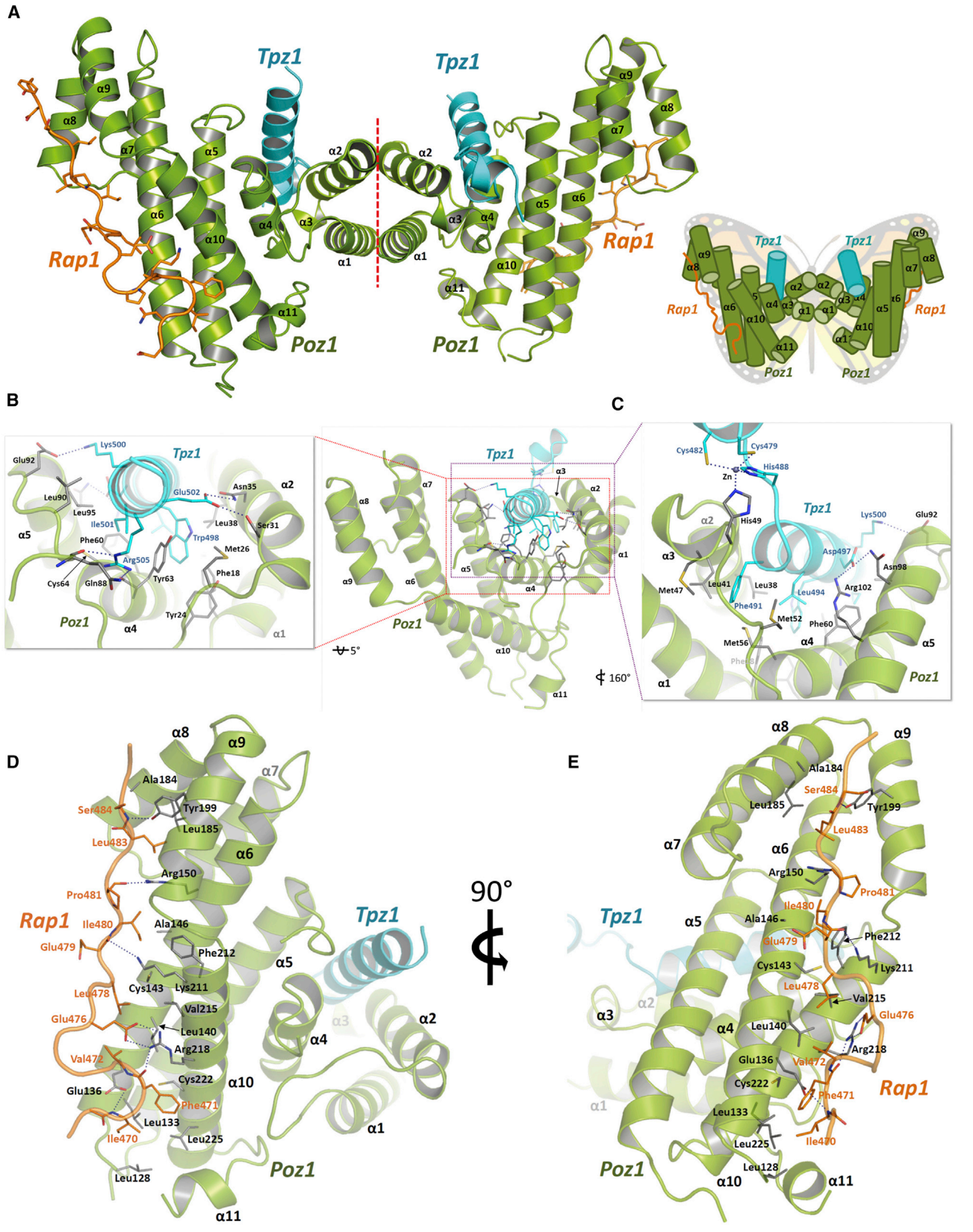

(legend on next page)

complex. To facilitate the crystallization of Tpz1-Poz1-Rap1 complex, we first mapped the Rap1 region that is both necessary and sufficient for its binding to Tpz1-Poz1 (Figure S2A). A number of combinations of Tpz1, Poz1, and Rap1 constructs were trialed for crystallization of the complex, and finally Tpz1$^{475-508}$-Poz1-Rap1$^{467-496}$ produced high-quality crystals. With these crystals, we determined the crystal structure of Tpz1$^{475-508}$-Poz1-Rap1$^{467-496}$ complex using SAD (single-wavelength anomalous dispersion) at 2.3 Å resolution (STAR Methods; Table 1). As shown in Figure 2A, the Tpz1$^{475-508}$-Poz1-Rap1$^{467-496}$ complex forms a dimer in the crystal, showing a compact, butterfly-shaped structure consisting mainly of α helices. Two Poz1 molecules, each containing eleven α helices, build the "body" and the "wings" of the butterfly, with two Tpz1 molecules standing out as the "antennas." Each Rap1 molecule lies around the edge of the butterfly "wing." Helices α1 and α2 from each Poz1 interact with each other in an anti-parallel manner, forming the dimer interface of the complex, analogous to the "body" part of the butterfly. The dimerization interface is composed of eleven residues from α1 and α2, covering 707.2 Å^2 surface area (Figure S2B). In accordance with the dimer observed in the crystal structure, the Tpz1$^{475-508}$-Poz1-Rap1$^{467-496}$ complex was eluted at the dimer volume when purified by the gel-filtration chromatography (Figure S2C) and was determined to have dimer mass by size-exclusion chromatography-multi-angle light scattering (SEC-MALS) in solution (Figure S2D). The rest of the eight α helices (α3–α11) of Poz1 are arranged into a multi-helix bundle, resembling the butterfly "wing." Importantly, it is evident that Tpz1 and Rap1 bind to distinctively different locations on Poz1, and no direct contact is observed between Tpz1$^{475-508}$ and Rap1$^{467-496}$, supporting the allosteric mechanism.

In the Tpz1$^{475-508}$-Poz1-Rap1$^{467-496}$ complex, Tpz1$^{475-508}$ adopts a helix-turn-helix structure and inserts its longer helix into the concave formed by helices α2, α3, α4, and α5 of Poz1 (Figures 2B and 2C). The interaction between Tpz1 and Poz1 involves an extended hydrophobic core composed of four hydrophobic residues from Tpz1—Phe491, Leu494, Trp498, and Ile501—intertwining with a number of hydrophobic residues on Poz1. Specifically, Phe491 and Leu494 of Tpz1 sit in a pocket formed by Leu38, Leu41, Met47, Met52, Met56, and Phe60 of Poz1. The aromatic ring of Trp498 in Tpz1 interacts with that of Tyr63 in Poz1 via π-π stacking. In addition, Trp498 also has hydrophobic interactions with Phe18, Tyr24, Met26, Leu38, and Tyr63 of Poz1. Tpz1-Ile501, a previously identified key residue for Tpz1-Poz1 interaction (Jun et al., 2013), is surrounded by Phe60, Tyr63, and Cys64 from α4, together with Leu90 and Leu95 from α5 of Poz1. Therefore, the four hydrophobic residues from Tpz1 mimic "key teeth," sticking into the shape-complemented convex formed by hydrophobic residues of Poz1 (Figure S2E). Around the hydrophobic interior, there are a number of salt bridges formed between Tpz1 and Poz1, for example, Asp497 of Tpz1 with Asn98 and Arg102 of Poz1, Lys500 of Tpz1 with Glu92 of Poz1, Glu502 of Tpz1 with Ser31 and Asn35 of Poz1, and Arg505 of Tpz1 with the backbone C = O groups of Poz1, Tyr63, and Gln88 (Figures 2B, 2C, and S2F). Interestingly, we also observed a zinc ion existing at the Tpz1-Poz1 interface, coordinated by Cys479, Cys482, and His488 of Tpz1, and His49 of Poz1 with a tetrahedral conformation (Figure 2C).

On the opposite side of the Tpz1-binding region in the Tpz1$^{475-508}$-Poz1-Rap1$^{467-496}$ complex, Rap1 exists in an extended conformation and packs into a long groove in Poz1 created by its helices α8, α9, and α10 turning around helix α6 (Figures 2D and 2E). Rap1 interacts with Poz1 in an unusual way, consisting of two separate hydrophobic cores that anchor Rap1 to Poz1, burying a total of 918 Å of solvent-accessible area of each protein. In the first hydrophobic core, Ile470, Phe471, Val472, Leu478, and Ile480 from Rap1 have extensive hydrophobic interactions with Leu128, Leu133, Leu140, Cys143, Ala146, Phe212, Val215, Cys222, and Leu225 of Poz1. The second hydrophobic core is built by Leu483 of Rap1, interacting with Ala184, Leu185, and Tyr199 of Poz1. Located in between these two hydrophobic cores is a region of Poz1 carrying overall positive surface potential (Figure S2G). In fact, specific recognition of Rap1 by Poz1 is aided by multiple hydrogen bonds formed between the backbone of Rap1 and of Poz1 with side chains from α6 (Glu136 and Arg150) and α10 (Lys211 and Arg218) in this mostly positively charged region of Poz1. In addition, a salt bridge is also observed between side chains of Rap1-Glu476 and Poz1-Arg218. Lastly, an aromatic-thiol π-type H-bond between Cys222 of Poz1 and Phe471 of Rap1 is formed in the Rap1-Poz1 interface (Figures 2D and 2E).

Taken together, based on the crystal structure of the Tpz1$^{475-508}$-Poz1-Rap1$^{467-496}$ complex, Tpz1 does not provide

Figure 2. Crystal Structure of the Tpz1-Poz1-Rap1 Complex

(A) Overall structure of the dimer form of Tpz1-Poz1-Rap1 complex, colored according to shelterin schematic drawing in Figure 1A with Tpz1 in cyan, Poz1 in light green, and Rap1 in brown (left) and schematic representation of Tpz1-Poz1-Rap1 complex structure (right). Left: first two helices (α1 and α2) in the N terminus of Poz1 are involved in the dimerization of Tpz1-Poz1-Rap1 complex. Red dashed line indicates the dimer interface. Tpz1 was surrounded by five helices (α1, α2, α3, α4, and α5) of Poz1, located close to the dimerization interface. Rap1 binds to a long groove in Poz1 created by its helices α8, α9, and α10 turning around helix α6. Right: the outline of the dimer of Tpz1-Poz1-Rap1 complex resembling a butterfly shape. The position of each Tpz1 is at each antenna of the butterfly and the dimerization region of Poz1 forms the body part of the butterfly. Rap1-binding site is at the edge of each wing.

(B and C) Close-up views of Tpz1-Poz1 interface. (B) Hydrophobic core residue Trp498 interacts with Tyr63 by π-π stacking and is surrounded by hydrophobic residues Phe18, Tyr24, Met26, Leu38, and Tyr63 of Poz1. Glu502 forms H-bonds with Ser31 and Asn35 of Poz1. (C) Ile501 of Tpz1 is located in a hydrophobic core interacting with Phe60, Tyr63, Cys64, Leu90, and Leu95 of Poz1.

(D and E) Close-up views of Rap1-Poz1 interface. (D) Leu128, Leu133, Leu140, Cys222, and Leu225 of Poz1 provide a hydrophobic patch for the binding of Ile470, Phe471, and Val472 of Rap1. Arg218 in Poz1 is involved with H-bond with Glu476 of Rap1, which is located in the middle of Rap1. Phe471 of Rap1 interacts with Cys222 of Poz1 by aromatic-thiol π-type H-bond (3.8 Å). (E) Ile480 of Rap1 is located on the center of a hydrophobic core, which interacts with Cys143, Ala146, and Phe212 of Poz1. Leu478 of Rap1 interacts with Leu140, Cys143, and Val215 of Poz1. The side chain of Leu483 in Rap1 is surrounded by the hydrophobic residues Ala184, Leu185, and Tyr199 in Poz1. All figures for the structure presentations were generated with PyMol.

See Figure S2 and Table 1.

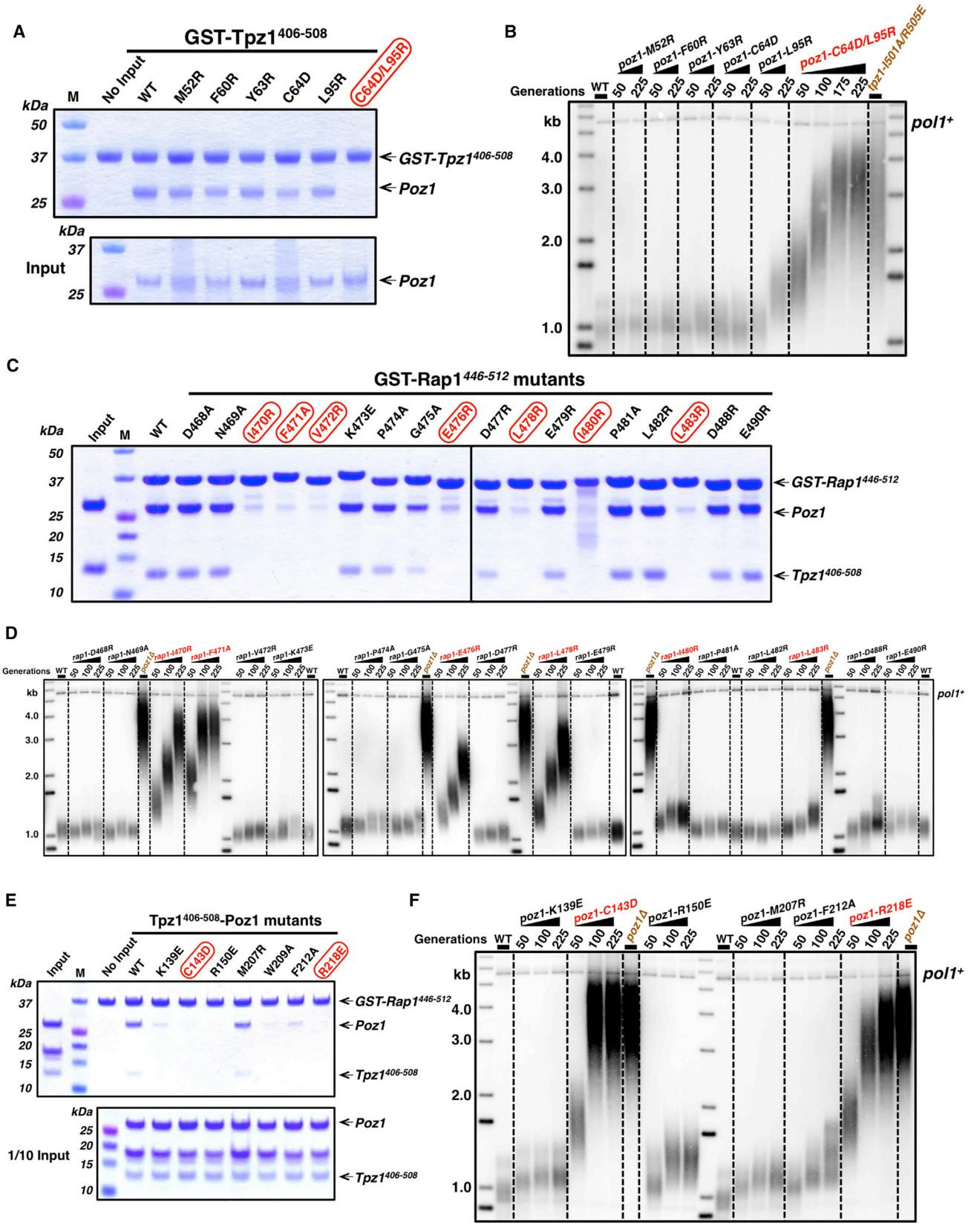

(legend on next page)

any additional binding surface for Rap1 and is located in a distinctively different site on Poz1 from Rap1. Thus, Tpz1-Poz1 interaction most likely triggers allosteric changes in Poz1 that lead to the formation of the high-affinity Rap1-binding groove.

Biochemical and Functional Analyses of the Tpz1-Poz1 Interface

To validate the observed interaction interface between Tpz1 and Poz1 in the crystal structure, we first employed GST pull-down assays to evaluate the binding of a panel of mutants targeting interface residues in Poz1. Interestingly, Poz1 single mutations of residues in the interface at most weakened, but did not disrupt, Tpz1-Poz1 interaction (Figure 3A). However, a double-mutant Poz1-C64D/L95R completely abolished Tpz1-Poz1 interaction in the GST pull-down assay (Figure 3A). This is reminiscent of what we observed previously for the Tpz1 mutants targeted to disrupt Tpz1-Poz1 interaction, in which only a double mutant of the Tpz1-Poz1 interface residues, Tpz1-I501A/R505E, completely disrupted Tpz1$^{406-508}$ -Poz1 interaction (Jun et al., 2013). This result indicates that the forces mediating Tpz1-Poz1 interaction along the interface are rather independent of each other, and therefore only combined mutations at different contact sites can lead to complete loss of Tpz1-Poz1 interaction. Furthermore, using co-immunoprecipitation, we confirmed that mutations abrogating Tpz1$^{406-508}$ and Poz1 interaction *in vitro* also disrupted the interaction between the full-length Tpz1 and Poz1 (Figure S3A). In addition, these Poz1 mutants defective in Tpz1 binding cannot interact with Rap1 either, suggesting that, in cells, disturbing the Poz1-Tpz1 interface inhibits Poz1-Rap1 interaction. These results further support the proposed allosteric effect of Tpz1 on Poz1 being required for the formation of shelterin bridge-Tpz1-Poz1-Rap1 complex.

Next, we aimed to evaluate the functional outcome of disrupting Tpz1-Poz1 interaction by the *poz1*$^+$ mutant in telomere maintenance. We made a panel of *S. pombe* strains with the same set of Poz1 mutations as those in the binding assays. Among them, only *poz1-C64D/L95R* mutant cells had dramatically elongated telomeres, similarly to those of the previously characterized *tpz1*$^+$ mutant *tpz1-I501R/R505E* defective in Tpz1-Poz1 interaction (Jun et al., 2013) (Figure 3B). Together with our previous studies, this result not only validates the physiological relevance of the Tpz1-Poz1 interface observed in the crystal structure, but it also reconfirms the importance of the integrity of the shelterin bridge in proper telomeric state regulation.

Biochemical and Functional Analyses of the Poz1-Rap1 Interface

We further assessed the extended Poz1-Rap1 interaction interface by mutational scanning of Rap1 residue interface based on the Tpz1$^{475-508}$-Poz1-Rap1$^{467-496}$ crystal structure. We utilized GST pull-down assay to evaluate the binding efficiency between Rap1 mutants and Poz1-Tpz1 complex *in vitro*. As expected, Rap1 point mutations of residues comprising each of the two hydrophobic interaction cores, with I470R, F471A, V472R, L478R, and I480R targeting the first, and L483R targeting the second, were able to completely disrupt Rap1$^{446-512}$-Poz1 interaction (Figure 3C). Moreover, Rap1-E476R, a mutant that disrupts a salt bridge between Rap1-Glu476 and Poz1-Arg218, also led to loss of Rap1-Poz1 interaction (Figure 3C). Correspondingly, Poz1 point mutations that either compromise the hydrophobic interaction core (C143D and F212A) or disrupt the salt bridges (K139E, R150E, and R218E) were also able to fully disrupt or severely weaken Poz1-Rap1 interaction (Figure 3D). Our co-immunoprecipitation assays also confirmed the abrogation of full-length Poz1-Rap1 interaction caused by the same panel of Rap1 and Poz1 mutants (Figures S3B and S3C). Different from Tpz1-Poz1 interface, Poz1-Rap1 interaction appears to be mediated cooperatively by multiple hydrophobic interactions and salt bridges, and as a result, disruption of any one of these forces leads to the complete breakdown of the interaction.

Similarly, to test the *in vivo* consequence of the Poz1-Rap1 interaction in telomere length maintenance, we generated yeast strains carrying the same set of *rap1*$^+$ or *poz1*$^+$ point mutations as those used in the binding assays. Along the extended Poz1-Rap1 interaction interface, the disruption of the core residues in the hydrophobic patches of Rap1 (*rap1-I470R*, *rap1-F471A*, *rap1-L478R*, and *poz1-C143D*) and residues forming a salt bridge (*rap1-E476R* and *poz1-R218E*) (Figures 3E and 3F) resulted in unregulated telomere elongation, similar to the *poz1Δ* strain. Moreover, other mutants that weakened Poz1-Rap1 interaction also caused telomere elongation to different degrees, in accordance with the severity of Poz1-Rap1 interaction defect. Taken together, these results functionally verified Poz1-Rap1 interface structure and signified its role in telomere length regulation.

Tpz1 Binding Induces the Folding of the N-Terminal Helix α1 of Poz1

To elucidate the mechanism by which Tpz1-Poz1 interaction enhances Poz1-Rap1 interaction, we aimed to probe the possible

Figure 3. Dissection of Tpz1-Poz1-Rap1 Interfaces and Dramatic Telomere Elongation Caused by Interface Mutations

(A) *In vitro* GST pull-down assays evaluating the binding of Poz1 mutants to GST-Tpz1$^{406-508}$. A double mutant of Poz1, Poz1-C64D/L95R (colored in red), is defective in binding to GST-Tpz1$^{406-508}$. Input: 1/15 of the samples before their incubation with GST-Tpz1$^{406-508}$.

(B) Telomere length analysis of indicated *poz1* mutant strains from successive re-streaks on agar plates by southern blotting. The telomere fragment is released from total genomic DNA by EcoRI digestion. *tpz1-3Flag* serves as wild-type control and is denoted as "WT"; *tpz1-I501A/R505E* (colored in brown) is a previously identified mutant defective in Poz1-Tpz1 interaction and thus serves as a control. In this paper, the 1 kb plus marker (from Life Technologies) is used in all telomere length analyses. *pol1*$^+$ indicates an EcoRI digested *pol1*$^+$ gene fragment, which was used as the loading control.

(C and E) *In vitro* GST pull-down assays evaluating the bindings of GST-Rap1$^{446-512}$ mutants to Tpz1$^{406-508}$-Poz1 complex (C), and conversely, Tpz1$^{406-508}$-Poz1 mutants to GST-Rap1$^{446-512}$ (E). The mutants that disrupt Poz1-Rap1 interaction are colored in red. Input: 1/10 of Tpz1$^{406-508}$-Poz1 complex, either wild-type or mutants, before their incubation with GST-Rap1$^{446-512}$.

(D and F) Telomere length analysis of indicated *rap1* mutant strains (D) or *poz1* mutants strains (F) from successive re-streaks on agar plates by southern blotting. The telomere fragment is released from genomic DNA by EcoRI digestion. *rap1-WT-3Flag* (D) or *poz1-WT-13myc* (F) is denoted as "WT" in the telomere blot. See Figure S3.

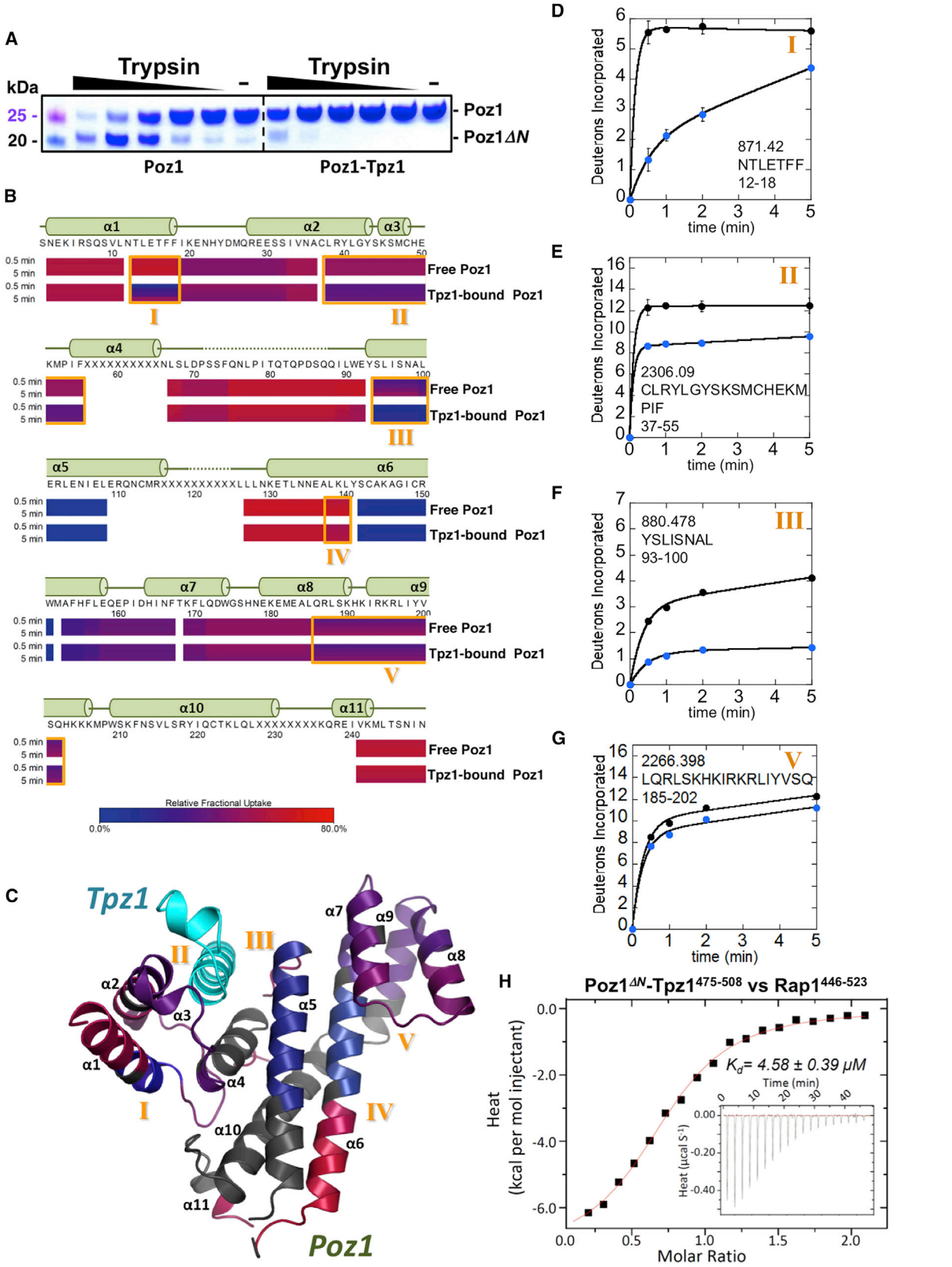

(legend on next page)

conformational changes in Poz1 upon its binding to Tpz1. We thus carried out a limited proteolysis assay to probe the protein flexibility of free Poz1 and Tpz1-bound Poz1. As shown in Figure 4A, the Poz1-Tpz1 complex was trypsin proteolysis resistant, whereas Poz1 alone was proteolyzed to a lower molecular weight product. Mass spectrometry sequencing of the lower molecular weight band identified it as Poz1 missing its N-terminal helix α1, denoted as Poz1*ΔN*. Therefore, the binding of Tpz1 to Poz1 is likely to induce the folding of the flexible N-terminal helix α1. To further understand the folding process of Poz1 helix α1 upon Tpz1 binding to Poz1, we employed amide hydrogen/deuterium exchange detected by mass spectrometry (HXMS) to probe the solvent accessibility of amide protons, enabling comparison of the folded states of free Poz1 and Tpz1-bound Poz1 (Balasubramaniam and Komives, 2013). The exchange rates of amide protons measured by HXMS vary from milliseconds for amides in unstructured peptides to days for amides in cores of globular proteins. As shown in Figure 4B, pepsin digestion of both free Poz1 and Tpz1-bound Poz1 yielded 34 peptides covering 75% of the Poz1 sequence. Poz1 appears to have a wide range of different exchange properties: much of it is exchanging nearly all of its amides (Figure S4A), and then there are a few regions that exchange very little (Figure S4B). Interestingly, whereas most regions in Poz1 have similar exchange in its free and Tpz1-bound forms, there are three regions that show distinctly decreased exchanges, and two regions that show moderately decreased exchanges upon Tpz1 binding to Poz1 (Figures 4B and 4C). Among these five regions, the most dramatic one is a peptide covering residues 12 to18, representing the second half of helix α1 (Figures 4B and 4C). In the free form, this part of Poz1 readily exchanges almost all of its amide protons for deuterons, suggesting the unstructured nature of this region (Figure 4D). However, this exchange dramatically reduces upon Tpz1 binding to Poz1 (Figure 4D), indicating that helix α1 becomes folded when bound to Tpz1. This HXMS result is highly correlated with the crystal structure of Tpz1$^{475\text{-}508}$-Poz1-Rap1$^{467\text{-}496}$ complex, in which α1 of Poz1 is packed against α2, α3, and α4. Accordingly, another peptic peptide with decreased exchange rate in Tpz1-bound Poz1 covers residues 37 to 55 (Figure 4E), which include the end of α2, α3, and the very beginning of α4—all closely contacting the newly formed α1 upon Tpz1 binding (Figure 4C). Amide proton exchange is also sensitive to changes in protection at the binding interface. From the crystal structure, we can see that Tpz1 interacts with the other side of α2, α3, and α4 region, together with α1 contributing to the decreased exchange. In addition, another contact side for Tpz1 in Poz1, located at the very end of α5 consisting of residues 93–100, also shows less deuterium incorporation when Tpz1 is bound to Poz1 (Figure 4F). In two more distal regions from the Tpz1-binding site of Poz1, covering residues 138–140 and 185–202, moderate levels of decrease in deuterium incorporation were also observed (Figures S4C and 4G). These two regions fall into the Rap1-binding site of Poz1, based on the crystal structure of the Tpz1$^{475\text{-}508}$-Poz1-Rap1$^{467\text{-}496}$ complex (Figures 2D and 2E). These results directly demonstrate the allosteric structural changes in the Rap1-binding region of Poz1 induced by the binding of Tpz1 to Poz1. Therefore, our limited proteolysis and HXMS experiments both suggest that Tpz1 binding to Poz1 prompts the conformational changes in Poz1, which include the folding of its N-terminal helix and other structural changes propagated from it, thus resulting in a high-affinity binding site for Rap1.

We next asked whether the induced folding of Poz1 N-terminal helix α1 upon Tpz1-Poz1 interaction is required for the enhanced Poz1-Rap1 interaction. Consistent with this hypothesis, our ITC data indicated that Poz1*ΔN* (Poz1$^{29\text{-}249}$), even in the presence of Tpz1, interacts with Rap1 with K_d of 4.58 μM (Figure 4H), similar to that of Poz1-Rap1 interaction without Tpz1 (K_d = 5.62 μM). Moreover, our real-time binding kinetics analysis using BLI indicated that the binding kinetics (k_{on} and k_{off}) of the interaction between Rap1 and Tpz1-bound Poz1*ΔN* are very similar to that of Rap1 and free Poz1*ΔN* (Figures S4D and S4E). Therefore, given that the crystal structure of the Tpz1$^{475\text{-}508}$-Poz1-Rap1$^{467\text{-}496}$ complex clearly shows that Rap1 binds to the C-terminal, instead of the N-terminal, region of Poz1 where Tpz1 binds, the N-terminal helix α1 most likely acts as a "conformational trigger," allosterically promoting Poz1 binding to Rap1 upon Tpz1-Poz1 interaction.

Structural Basis for the Allosteric Promotion of Poz1-Rap1 Interaction via the "Conformational Trigger"

Given the importance of the N-terminal helix α1 of Poz1 in stimulating Tpz1-bound Poz1 to interact with Rap1, we decided to elucidate the structural basis for the allosteric changes in Poz1 that enhance Poz1-Rap1 interaction via the "conformational trigger." To achieve this goal, we solved the crystal structure

Figure 4. Tpz1 Binding Induces the Folding of the N-Terminal Helix α1 of Poz1

(A) Limited proteolysis assay of free Poz1 and Tpz1-Poz1 complex in the presence of increasing trypsin concentration. While Poz1 was rather stable in the Tpz1-bound form, Poz1 alone was cleaved by trypsin and produced a band with lower molecular weight.

(B) Hydrogen-deuterium exchange mass spectrometry (HDXMS) analysis of free Poz1 and Tpz1-bound Poz1. Poz1 sequence is annotated by heatmaps below the sequence according to percent exchange after 0.5 and 5 min. Residues of Poz1 for which exchange is not reported are indicated as X's in the sequence and blank regions in heatmaps. The regions with lower deuterium exchange rate in Tpz1-bound Poz1 than that of free Poz1 are boxed with orange color (I, II, III, IV, and V). Secondary structure elements of Poz1 are indicated above the sequence.

(C) Poz1 structure in the Tpz1-Poz1 complex is colored based on its exchange rate measured in the Tpz1-bound state as shown in (B). Regions with no exchange data reported are colored gray in the Poz1 structure. Tpz1 is colored cyan.

(D–G) Amide hydrogen-deuterium exchange in Poz1 with and without Tpz1. The graphical data of deuterium incorporation in Poz1 show differences between free Poz1 (black dot) and Tpz1-bound Poz1 (blue dot) in I (D), II (E), III (F), and V (G) regions of (B). Error bars indicate SD (n = 3).

(H) ITC measurement of the affinity between Tpz1$^{475\text{-}508}$-Poz1Δ*N* complex and Rap1$^{446\text{-}523}$ The binding affinity of Tpz1$^{475\text{-}508}$-Poz1Δ*N* complex-Rap1$^{446\text{-}523}$ interaction (4.58 μM) is similar to that of free Poz1-Rap1$^{446\text{-}523}$ interaction (5.62 μM). Insert is the titration data, with the K_d value ± SD calculated from the fit shown above it. ITC experiments were repeated twice and representative results were shown.

See Figure S4.

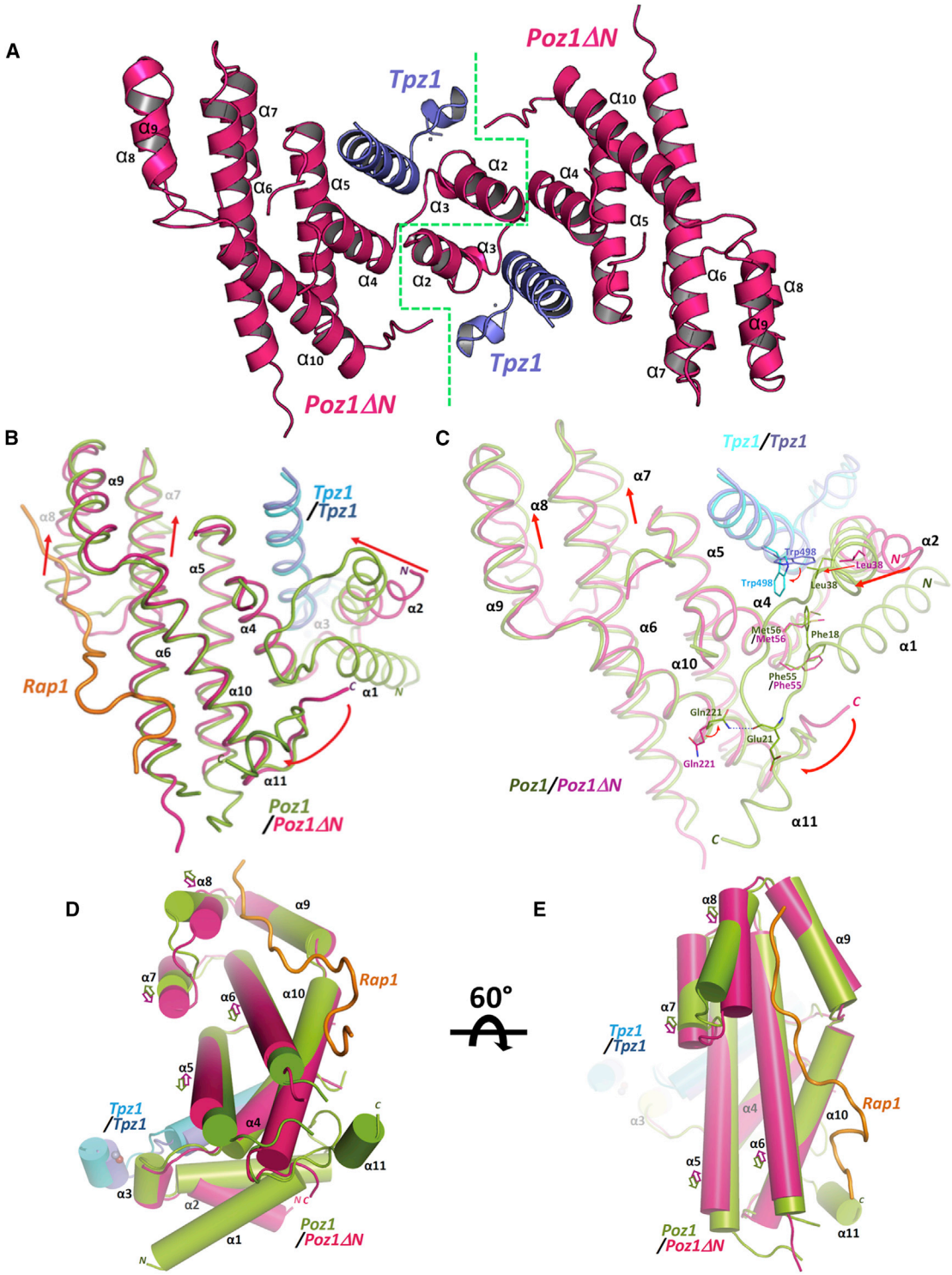

Figure 5. Structural Comparison of Tpz1-Poz1Δ*N* and Tpz1-Poz1 Complexes

(A) Overall structure of the dimer of Tpz1 (slate)-Poz1Δ*N* (hot pink) complex. Two helices of Poz1 (α2 and α3) comprise the dimerization interface. The green dashed line indicates the dimer interface.

(B) Superposition of Tpz1-Poz1Δ*N* and Tpz1-Poz1 complexes using C_α atoms. Conformational changes are observed in α2, α7, α8, and α11 of Poz1, indicated by red arrows. The RMSD (root-mean-square deviation) between the two structures is 1.29 Å.

(legend continued on next page)

of the Tpz1$^{475-508}$-Poz1ΔN complex, which enables the structural comparison to that of Tpz1$^{475-508}$-Poz1 structure in the Tpz1$^{475-508}$-Poz1-Rap1$^{467-496}$ complex. As shown in Figure 5A, Tpz1$^{475-508}$-Poz1ΔN forms a dimer of heterodimers. However, different from the dimer interface in Tpz1-Poz1, helices α2 from two Poz1ΔN molecules interact with each other in a "domain-swapped" manner, mediating the dimerization of Tpz1$^{475-508}$-Poz1ΔN complex. Our SEC-MALS measurement also indicated the dimer formation of Tpz1$^{475-508}$-Poz1ΔN complex in solution (Figure S5A). Based on the structure superposition (Figure 5B), the "conformational trigger"—N-terminal helix α1 of Poz1—imparts the movement of helix α2 toward Tpz1, which consequently induces the rotation of the side chain of Tpz1-Trp498, resulting in its packing against the side chain of Poz1-Leu38. In addition, folding of helix α1 creates new hydrophobic packing in Poz1 composed of Leu14, Phe18, Tyr24, Phe55, and Met56, providing structural explanations for the HXMS results. As demonstrated in a movie (Movies S1 and S2), based on the structures of the low-affinity and high-affinity Poz1, mostly likely due to the induced folding of α1 in Poz1 upon Tpz1 binding, α1 forms new hydrophobic packing with α4 and Glu21 in the loop connecting α1 and α2 forms hydrogen bonding with Gln221 in α10 (Figure 5C), which in turn triggers structural rearrangements in helices α6, α7, α8, and α9 to various degrees (Figures 5D and 5E). These Tpz1-binding-induced allosteric structural changes in Poz1 result in a more open binding groove for Rap1 (Figures S5B and S5C).

The "Conformational Trigger" in Poz1 Is Essential for Shelterin Assembly and Telomere Length Regulation

To assess the contribution of the "conformational trigger" in Poz1 to telomere maintenance, we introduced either Poz1 N-terminal deletion (*poz1-ΔN*) or several point mutations in helix α1 (*poz1-R6E*, *poz1-L14R*, and *poz1-F17A*) to *S. pombe* cells. Both *poz1-ΔN* and *poz1-L14R* strains had dramatically elongated telomeres, whereas *poz1-R6E* and *poz1-F17A* strains had wild-type telomere length (Figure 6A). From the crystal structure of Tpz1$^{475-508}$-Poz1-Rap1$^{467-496}$ complex, Leu14 in Poz1 α1 helix participates in the formation of the new hydrophobic packing against Leu38, Leu41 in α2, and Met56 in α4 (Figure S6A), and therefore, L14R mutation is most likely to disrupt the allosteric pathway that conveys Tpz1-Poz1 interaction-induced structure changes to the Rap1-binding region of Poz1. In contrast, residues Arg6 and Phe17 both point away from the new hydrophobic core (Figure S6A), and therefore their mutations have little effect on the "conformational trigger" function of α1 helix in Poz1. Consistent with our structural analysis and the telomere elongation phenotype of *poz1-L14R* strain, the binding affinity of Tpz1-bound Poz1-L14R interacting with Rap1 is the same as that of the free Poz1-Rap1 interaction (Figure 6B), similar to that of Tpz1-Poz1ΔN and Rap1 interaction (Figures 4H and S4C). In addition, the ~60-fold slower k_{off} observed in the association of Rap1 with Tpz1-bound Poz1 (compared to that of Rap1 with free Poz1) was not detected when L14R mutation was introduced to Tpz1-bound Poz1 (Figure 6B). Interestingly, in our co-immunoprecipitation assays, we observed full abrogation of Poz1-Rap1 interaction in both *poz1-ΔN* and *poz1-L14R* cells, whereas Rap1-Taz1 interaction was maintained at the wild-type level (Figure 6C). The protein levels of Poz1 were unchanged. To our surprise, in both *poz1-ΔN* and *poz1-L14R* cells, Tpz1-Poz1 interaction is also decreased about 3-fold, while Tpz1-Ccq1 interaction is still at the wild-type level in both mutant cells (Figure 6D). Our *in vitro* binding assays utilizing both BLI and ITC with purified recombinant proteins indicate that the binding affinity between Tpz1 and Poz1ΔN is similar to that of Tpz1 and wild-type Poz1 (Figures S6B and S6C).

To investigate the contribution of the "conformational trigger" in Poz1 to shelterin assembly on telomeres, we carried out chromatin immunoprecipitation (ChIP) analysis to investigate how Poz1 N-terminal deletion or mutation affects the telomeric localizations of Poz1 itself and other shelterin components. Whereas *poz1-ΔN* and *poz1-L14R* mutations only moderately decreased the telomeric localization of Rap1 (Figures 6E), these two mutations drastically diminished the enrichment of both Poz1 (Figure 6F) and Tpz1 (Figure 6G) on telomeres, indicating the critical role of the "conformational trigger" in Poz1 and the cooperativity it generates in promoting proper shelterin assembly on telomeres. For Tpz1, telomeric localization is still observed in both *poz1-ΔN* and *poz1-L14R* cells (Figure 6G); however, its enrichment along the elongated telomeres in these two mutant cells is low. The most likely explanation for this result is that Tpz1 is still recruited to telomeric G-overhang through Pot1, but the defective Tpz1-Poz1-Rap1 complex assembly in *poz1-ΔN* or *poz1-L14R* cells (Figure 6D) diminishes the recruitment of Tpz1 from the double-stranded telomeric DNA via Taz1-Rap1 interaction.

Cooperativity Is a Conserved Driving Force for Human Shelterin Assembly

Fission yeast shelterin is architecturally conserved to its human counterpart (Figure S7A). In both species, single-stranded telomeric DNA-binding complex—Tpz1/Pot1 in fission yeast and TPP1/POT1 in humans—is connected to telomeric duplex DNA binders—Taz1/Rap1 in fission yeast and TRF1/2/RAP1 in humans. Poz1 mediates the linkage in fission yeast by binding directly to Tpz1 and Rap1, whereas TIN2 links TPP1 to TRF2-RAP1 complex as well as to TRF1. We speculated whether there is a region existing in TRF2 equivalent to the Poz1-binding domain of fission yeast Rap1. We thus aligned the previously identified TIN2-binding domain of mammalian TRF2 to the Poz1-binding domain of fission yeast Rap1. Consistent with our speculation, we found significant conservation between these two regions from such diverged eukaryotes (Figure S7B). Moreover, based on the crystal structure of the Tpz1-Poz1-Rap1 complex, most of the conserved residues in Rap1 directly

(C) Close-up view of conformational changes induced by Poz1 "conformational trigger," helix α1, upon Tpz1 binding to Poz1.
(D and E) Two close-up views of the structural changes in the Rap1-binding site of Poz1. Tpz1 binding induces allosteric structural changes in Poz1, resulting in a more open binding groove for Rap1. The arrows indicate the directions of helix movements due to the structural changes.
See Figure S5 and Movies S1 and S2.

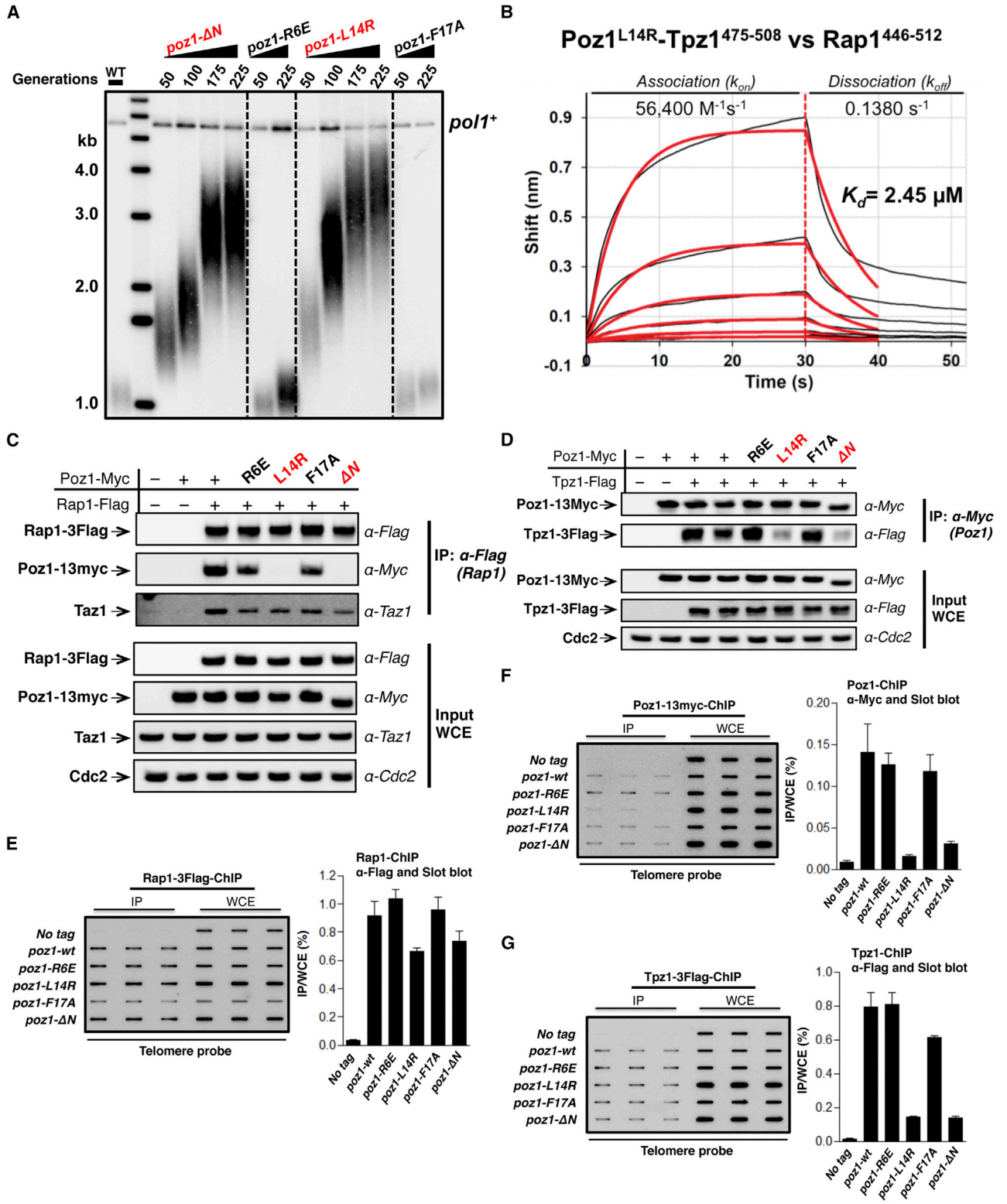

Figure 6. The "Conformational Trigger" in Poz1 Is Essential for Shelterin Assembly and Telomere Length Regulation

(A) Telomere length analysis of *poz1-NTD* mutant cells from successive re-streaks on agar plates. Total genomic DNA was digested by EcoRI. Wild-type cells are denoted as "WT" in the blot. Simultaneously digested *pol1*$^{+}$ DNA fragment serves as the loading control. Telomeres are elongated in *poz1-ΔN* and *poz1-L14R* cells (colored in red).

(legend continued on next page)

mediate the Rap1-Poz1 interaction. Next, we tested whether human TPP1-TIN2 interaction also enhances TIN2-TRF2 interaction, as fission yeast Tpz1-Poz1 interaction does to Poz1-Rap1 interaction. As shown in Figure 7A, our ITC measurements indicated that TRF2$^{382-424}$ binds to free TIN2 with a K_d of 3.11 μM, but it binds to TPP1$^{486-544}$-bound TIN2 with a K_d of 0.18 μM (Figure 7B), an 18-fold increase of binding affinity. Accordingly, our GST pull-down assay also demonstrated that GST-TRF2$^{42-446}$ binds to as low as 1 μM TPP1$^{486-544}$-bound TIN2 efficiently, whereas 30 μM of free TIN2 is required to achieve a similar level of binding (Figure S7C). Similar binding enhancement of TIN2-TRF2 interaction by TPP1 was also observed *in vivo* (O'Connor et al., 2006). Evidently, human shelterin bridge TPP1-TIN2-TRF2 also assembles in a similar hierarchical manner as its fission yeast counterpart, signifying cooperativity as a conserved driving force for shelterin assembly.

DISCUSSION

The Mechanism of Hierarchical Shelterin Bridge Assembly

Recent progress in dissecting the subunit interactions in the shelterin bridge and elucidating their functions has allowed a better understanding of how the shelterin complex acts to regulate telomere length homeostasis. The core of fission yeast shelterin is formed by a three-protein complex, consisting of Tpz1, Poz1, and Rap1 (Jun et al., 2013; Miyoshi et al., 2008; Pan et al., 2015). The Tpz1-Poz1-Rap1 complex has emerged as a key regulatory element of telomere synthesis by telomerase, based on its ability to bridge telomeric G-overhang-binding protein Pot1 to the telomeric duplex DNA-binding protein Taz1. Thus, key questions to understand telomere length control have been the shelterin bridge architecture, the molecular mechanism of the bridge formation, and the nature of shelterin assembly at telomeres. Our biochemical, structural, and functional analyses of the Tpz1-Poz1-Rap1 complex presented in this study reveal the hierarchical assembly of the shelterin bridge. This hierarchical assembly is enabled by the binary conformational change of Poz1 induced by Tpz1-Poz1 interaction, as illustrated in crystal structures of both the low- and high-affinity Rap1-binding modes of Poz1. Our characterizations of the cooperative shelterin bridge assembly at the atomic level coupled with *in vivo* functional analyses allow us to propose a model for shelterin assembly at telomeres. As depicted in Figure 7C, in fission yeast, Taz1 binds to telomeric dsDNA via its Myb DNA-binding domain, which in turn recruits Rap1 through protein-protein interaction. At the single-stranded G-overhang, about 30 nucleotides in length for *S. pombe*, Pot1 localizes to this region via the interaction between its N-terminal OB-fold domain and the G-overhang (Baumann and Cech, 2001; Erdel et al., 2017; Lei et al., 2003). The association of Tpz1 with Pot1 has been shown to increase the binding affinity with G-overhang ~10-fold (Nandakumar and Cech, 2012). Poz1 can be targeted to telomeres through its interaction with Tpz1, which triggers conformational changes in Poz1, thus making it bind to Rap1 with high affinity (Route I). As a result, a stable shelterin bridge linking telomeric dsDNA and ssDNA is formed via this stepwise, hierarchical assembly process, enforcing negative regulation on telomerase-mediated telomere elongation. On the other hand, Poz1 can also associate with chromatin-free Tpz1-Pot1 complex in the nucleus, turning into high-affinity Rap1-binding mode. Then, the Poz1-Tpz1-Pot1 complex is targeted to telomeres through associating with the Taz1-Rap1 complex located at telomeres (Route II).

Structural Features of the Shelterin Bridge

The crystal structure of the Tpz1$^{475-508}$-Poz1-Rap1$^{467-496}$ complex, determined at 2.3 Å resolution, represents the atomic structure of the shelterin bridge, a significant step forward in mechanistic understanding of shelterin functions. The binding of Tpz1 to Poz1 induces the folding of the critical "conformational trigger," N-terminal helix α1 of Poz1, and the consequent structural changes propagated to the Rap1-binding region of Poz1. Both Tpz1-Poz1 and Rap1-Poz1 interaction interfaces appear to be uniquely tailored for the cooperative assembly process. Cooperativity ensures that the whole complex is more stable than the sum of its parts (Williamson, 2008), and our crystal structures illustrate the structural basis for the cooperative assembly. The interaction between Tpz1 and Poz1 relays on a wide and continuous hydrophobic interface. This strong and stable hydrophobic interaction induces committed structure changes in Poz1, including those at its Rap1-binding sites. Our HXMS analysis revealed a high degree of plasticity in free Poz1, which facilitates its conformational changes immediately upon Tpz1 binding. The structure comparison of the low-affinity and high-affinity Rap1-binding states of Poz1 further reveals the detailed allosteric structural changes of Poz1 upon its binding to Tpz1. It also highlights the critical role of Poz1 helix α1—the "conformational trigger"—in promoting structural changes in Poz1 and in regulating shelterin bridge assembly. On the other hand, the Rap1-Poz1 interaction interface adopts a uniquely long and narrow shape, most likely to allow efficient sensing of the altered structural elements in Poz1 by Rap1. It is worth noting that there are two rather separated hydrophobic cores mediating Rap1-Poz1 interaction. Further specificity is provided by hydrogen bonding between the backbone of Rap1 and several side chains from Poz1. These structure features may facilitate the modular recognition of allosteric

(B) Bio-layer interferometry (BLI) sensorgrams monitoring dissociation and association events in real time between Poz1^{L14R}-Tpz1$^{475-508}$ and Rap1$^{446-512}$ using Octet red96 (R^2 = 0.9949). BLI experiments were repeated twice and representative results were shown.

(C and D) Co-immunoprecipitation assays evaluating the effect of Poz1 N-terminal helix deletion or mutation on Taz1-Rap1, Poz1-Rap1 (C), and Tpz1-Poz1 (D) interactions. Poz1-Rap1 interaction is fully disrupted in *poz1-ΔN* and *poz1-L14R* cells, whereas Poz1-Tpz1 interaction is weakened in *poz1-ΔN* and *poz1-L14R* cells. Rap1-Taz1 interaction remains unchanged.

(E–G) Telomeric localization of Rap1 (E), Poz1 (F), and Tpz1 (G) in strains with Poz1 N-terminal helix deletion or mutation was monitored by chromatin immunoprecipitation (ChIP) assay. Slot blot hybridized with telomere probe was used to visualize the telomeric signal associated with each protein. Each ChIP assay was performed in triplicate (n = 3). Error bars represent SDs.

See Figure S6.

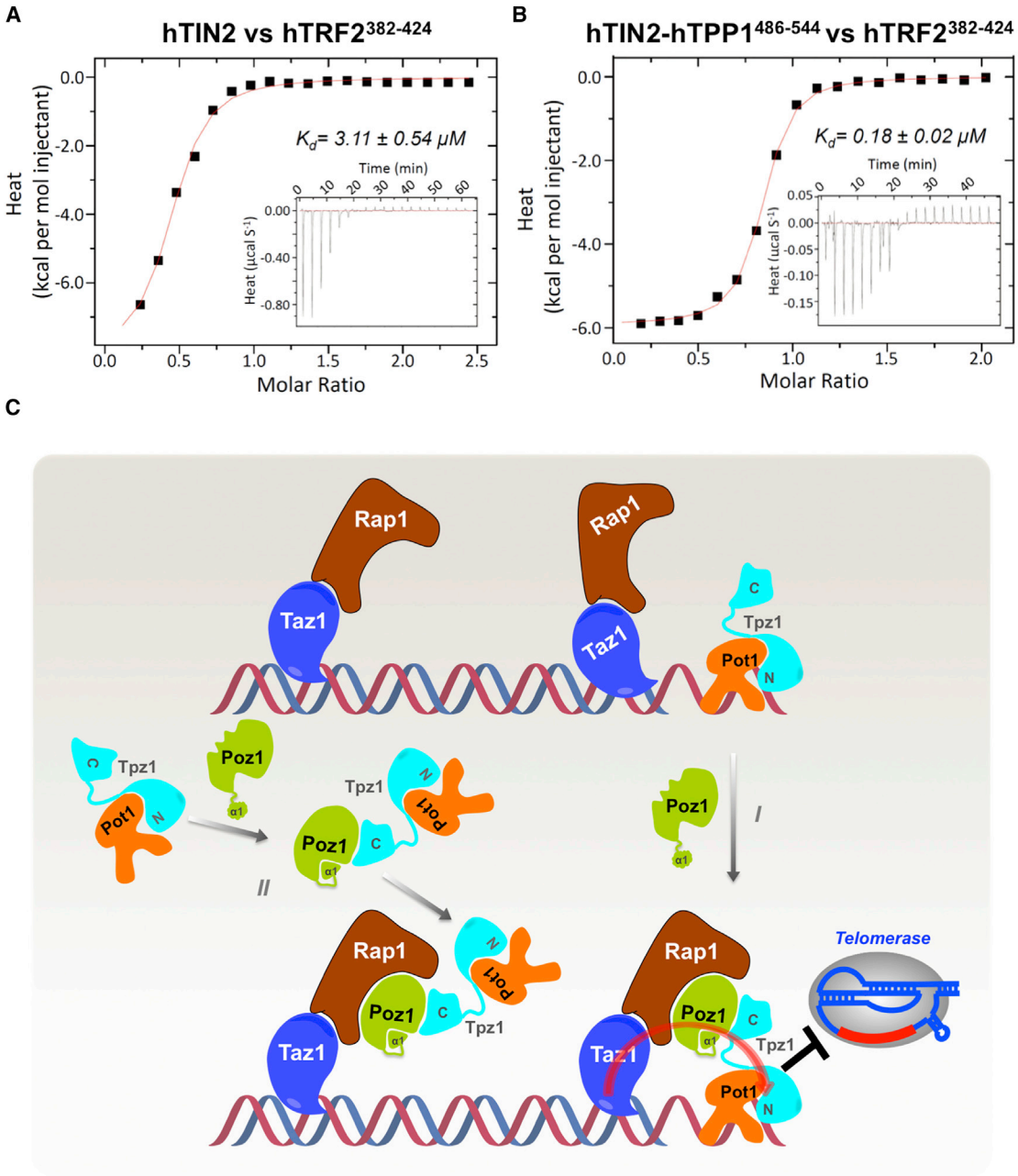

Figure 7. Conserved Driving Force for Cooperativity of Human Shelterin Assembly

(A and B) ITC measurements of interactions between human shelterin components hTIN2 and hTRF2$^{382-424}$ (A), and hTIN2-hTPP1$^{486-544}$ complex and hTRF2$^{382-424}$ (B). The binding of hTPP1$^{486-544}$ to hTIN2 increases the binding affinity of hTIN2-hTRF2$^{382-424}$ more than ~17-fold. Insert is the titration data, with the K_d value ± SD calculated from the fit shown above it. ITC experiments were repeated twice and representative results were shown.

(C) The schematic model of hierarchical shelterin complex assembly at telomeres in fission yeast.

See Figure S7.

changes in Poz1 and thus achieve effective coupling of Tpz1-Poz1 binding to Poz1-Rap1 binding to form a stable shelterin bridge.

Implications for the Regulation of Telomere Elongation

Previous studies support the model that the shelterin bridge between the double-stranded and single-stranded telomeric DNA is critical for maintaining telomere length by controlling the telomere state and regulating the accessibility of telomerase to telomeres (Jun et al., 2013; Pan et al., 2015). Accurate and stable shelterin bridge assembly is essential for this important shelterin function. Our work reported here provides the atomic-level structural view of the shelterin bridge and its cooperative

assembly mechanism. The cooperativity ensures that the binding between shelterin components is connected through the structure, which warrants that the whole Tpz1-Poz1-Rap1 complex is more stable than the sum of its parts, thereby driving the complex assembly, in a similar manner as many other macromolecular complexes, such as ribosomes (Mizushima and Nomura, 1970; Talkington et al., 2005). On the other hand, the cooperative mechanism also enables rapid disassembly of the shelterin bridge by disrupting a key element in the complex assembly, thus achieving timely switching from telomerase-nonextendible to -extendible state of telomeres. Indeed, our co-immunoprecipitation assays show that either a mutation in or a deletion of the "conformational trigger" in Poz1 leads to a greater degree of disruption of Tpz1-Poz1-Rap1 complex than it causes in binding assays (ITC or BLI) using the purified recombinant proteins. Since co-immunoprecipitation monitors interactions between endogenous proteins in the cell, which can bear regulatory post-translational modifications (PTMs), it is possible that loss of the "conformational trigger" in Poz1 elicits PTMs on Poz1, which further inhibit Poz1-Rap1 and Poz1-Tpz1 interactions.

STAR★METHODS

Detailed methods are provided in the online version of this paper and include the following:

- KEY RESOURCES TABLE
- CONTACT FOR REAGENT AND RESOURCE SHARING
- EXPERIMENTAL MODEL AND SUBJECT DETAILS
  - *E. coli* Rosetta (DE3) and BL21(DE3)
  - *E. coli* XL10-Gold
  - *S. pombe*
- METHOD DETAILS
  - Protein expression and purification
  - Crystallization, data collection and structure determination
  - Yeast Strains, Gene Tagging, and Mutagenesis
  - GST-pulldown assay
  - Telomere Length Analysis
  - Co-Immunoprecipitation
  - Isothermal Calorimetry (ITC)
  - Biolayer Interferometry (BLI) and K_d Calculation
  - Size-Exclusion Chromatograph-Multi-Angle Light Scattering (SEC-MALS)
  - Hydrogen/deuterium exchange mass spectrometry (HXMS)
- QUANTIFICATION AND STATISTICAL ANALYSIS
- DATA AND SOFTWARE AVAILABILITY

SUPPLEMENTAL INFORMATION

Supplemental Information includes seven figures, two tables, and two movies and can be found with this article online at https://doi.org/10.1016/j.molcel.2017.10.032.

AUTHOR CONTRIBUTIONS

F.Q. conceived, designed, and supervised the study. J.-K.K. and J.L. made various constructs, purified the proteins, and crystallized the complexes. J.-K.K. and B.S. collected diffraction data. J.-K.K. solved and refined the crystal structures. J.L. performed biochemical and genetic experiments and analyzed the data. X.H. performed the ChIP assays. E.A.K. performed the HXMS experiment and analyzed the data. C.Y. and L.H. performed mass spectrometry analysis of the limited proteolysis. K.R. and J.L. performed SEC-MALS analyses. J.L., J.-K.K., and E.A.K. prepared the figures. F.Q. wrote the manuscript with input from J.L., J.-K.K., and E.A.K.

ACKNOWLEDGMENTS

This paper is dedicated to Dr. Masayasu Nomura, whose laboratory space we inherited and whose pioneering work on ribosome assembly inspired our initial hypothesis for the hierarchical assembly of telomeric shelterin complex reported here. We thank Fuyuki Ishikawa, Toru Nakamura, Julie Cooper, Virginia Zakian, Pingwei Li, and Takashi Toda for generously providing plasmids, strains, or antibodies, and Peter Kaiser and Craig Kaplan for comments on the manuscript and helpful discussions. This work was supported by NIH grant R01GM098943 and American Cancer Society Research Scholar grant RSG-16-041-01-DMC to F.Q., as well as R01GM074830 and R01GM106003 to L.H. We would like to acknowledge Laser Spectroscopy Laboratories at UC Irvine, the excellent management by its director Dr. Dmitry Fishman, and NIH grant OD021594. The Berkeley Center for Structural Biology is supported in part by the NIH, National Institute of General Medical Sciences, and the Howard Hughes Medical Institute. The Advanced Light Source is supported by the Director, Office of Science, Office of Basic Energy Sciences, of the United States Department of Energy under contract no. DE-AC02-05CH11231. SSRL SMB program is supported by the DOE-BES, DOE-BER, NIH, NIGMS (P41GM103393).

Received: June 12, 2017
Revised: August 16, 2017
Accepted: October 23, 2017
Published: November 16, 2017

REFERENCES

Adams, P.D., Afonine, P.V., Bunkóczi, G., Chen, V.B., Davis, I.W., Echols, N., Headd, J.J., Hung, L.W., Kapral, G.J., Grosse-Kunstleve, R.W., et al. (2010). PHENIX: a comprehensive Python-based system for macromolecular structure solution. Acta Crystallogr. D Biol. Crystallogr. *66*, 213–221.

Afonine, P.V., Grosse-Kunstleve, R.W., Echols, N., Headd, J.J., Moriarty, N.W., Mustyakimov, M., Terwilliger, T.C., Urzhumtsev, A., Zwart, P.H., and Adams, P.D. (2012). Towards automated crystallographic structure refinement with phenix.refine. Acta Crystallogr. D Biol. Crystallogr. *68*, 352–367.

Artandi, S.E., and Cooper, J.P. (2009). Reverse transcribing the code for chromosome stability. Mol. Cell *36*, 715–719.

Autexier, C., and Lue, N.F. (2006). The structure and function of telomerase reverse transcriptase. Annu. Rev. Biochem. *75*, 493–517.

Baerlocher, G.M., Oppliger Leibundgut, E., Ottmann, O.G., Spitzer, G., Odenike, O., McDevitt, M.A., Röth, A., Daskalakis, M., Burington, B., Stuart, M., and Snyder, D.S. (2015). Telomerase inhibitor imetelstat in patients with essential thrombocythemia. N. Engl. J. Med. *373*, 920–928.

Bähler, J., Wu, J.Q., Longtine, M.S., Shah, N.G., McKenzie, A., 3rd, Steever, A.B., Wach, A., Philippsen, P., and Pringle, J.R. (1998). Heterologous modules for efficient and versatile PCR-based gene targeting in Schizosaccharomyces pombe. Yeast *14*, 943–951.

Balasubramaniam, D., and Komives, E.A. (2013). Hydrogen-exchange mass spectrometry for the study of intrinsic disorder in proteins. Biochim. Biophys. Acta *1834*, 1202–1209.

Batista, L.F., and Artandi, S.E. (2013). Understanding telomere diseases through analysis of patient-derived iPS cells. Curr. Opin. Genet. Dev. *23*, 526–533.

Battye, T.G., Kontogiannis, L., Johnson, O., Powell, H.R., and Leslie, A.G. (2011). iMOSFLM: a new graphical interface for diffraction-image processing with MOSFLM. Acta Crystallogr. D Biol. Crystallogr. *67*, 271–281.

Baumann, P., and Cech, T.R. (2001). Pot1, the putative telomere end-binding protein in fission yeast and humans. Science *292*, 1171–1175.

Bernardes de Jesus, B., and Blasco, M.A. (2013). Telomerase at the intersection of cancer and aging. Trends Genet. *29*, 513–520.

Cohn, M., and Blackburn, E.H. (1995). Telomerase in yeast. Science *269*, 396–400.

Collins, K. (2006). The biogenesis and regulation of telomerase holoenzymes. Nat. Rev. Mol. Cell Biol. *7*, 484–494.

Cooper, J.P., Nimmo, E.R., Allshire, R.C., and Cech, T.R. (1997). Regulation of telomere length and function by a Myb-domain protein in fission yeast. Nature *385*, 744–747.

de Lange, T. (2005). Shelterin: the protein complex that shapes and safeguards human telomeres. Genes Dev. *19*, 2100–2110.

Emsley, P., Lohkamp, B., Scott, W.G., and Cowtan, K. (2010). Features and development of Coot. Acta Crystallogr. D Biol. Crystallogr. *66*, 486–501.

Erdel, F., Kratz, K., Willcox, S., Griffith, J.D., Greene, E.C., and de Lange, T. (2017). Telomere recognition and assembly mechanism of mammalian shelterin. Cell Rep. *18*, 41–53.

Ferreira, M.G., Miller, K.M., and Cooper, J.P. (2004). Indecent exposure: when telomeres become uncapped. Mol. Cell *13*, 7–18.

Fujita, I., Tanaka, M., and Kanoh, J. (2012). Identification of the functional domains of the telomere protein Rap1 in Schizosaccharomyces pombe. PLoS ONE *7*, e49151.

Greider, C.W., and Blackburn, E.H. (1985). Identification of a specific telomere terminal transferase activity in Tetrahymena extracts. Cell *43*, 405–413.

Greider, C.W., and Blackburn, E.H. (1987). The telomere terminal transferase of Tetrahymena is a ribonucleoprotein enzyme with two kinds of primer specificity. Cell *51*, 887–898.

Günes, C., and Rudolph, K.L. (2013). The role of telomeres in stem cells and cancer. Cell *152*, 390–393.

Harley, C.B. (2008). Telomerase and cancer therapeutics. Nat. Rev. Cancer *8*, 167–179.

Hiyama, E., and Hiyama, K. (2007). Telomere and telomerase in stem cells. Br. J. Cancer *96*, 1020–1024.

Hu, X., Liu, J., Jun, H.I., Kim, J.K., and Qiao, F. (2016). Multi-step coordination of telomerase recruitment in fission yeast through two coupled telomere-telomerase interfaces. eLife *5*, e15470.

Jain, D., and Cooper, J.P. (2010). Telomeric strategies: means to an end. Annu. Rev. Genet. *44*, 243–269.

Jun, H.I., Liu, J., Jeong, H., Kim, J.K., and Qiao, F. (2013). Tpz1 controls a telomerase-nonextendible telomeric state and coordinates switching to an extendible state via Ccq1. Genes Dev. *27*, 1917–1931.

Lansdorp, P.M. (2005). Role of telomerase in hematopoietic stem cells. Ann. N Y Acad. Sci. *1044*, 220–227.

Lei, M., Podell, E.R., Baumann, P., and Cech, T.R. (2003). DNA self-recognition in the structure of Pot1 bound to telomeric single-stranded DNA. Nature *426*, 198–203.

Liu, J., Yu, C., Hu, X., Kim, J.K., Bierma, J.C., Jun, H.I., Rychnovsky, S.D., Huang, L., and Qiao, F. (2015). Dissecting fission yeast shelterin interactions via MICro-MS links disruption of shelterin bridge to tumorigenesis. Cell Rep. *12*, 2169–2180.

Miyoshi, T., Kanoh, J., Saito, M., and Ishikawa, F. (2008). Fission yeast Pot1-Tpp1 protects telomeres and regulates telomere length. Science *320*, 1341–1344.

Mizushima, S., and Nomura, M. (1970). Assembly mapping of 30S ribosomal proteins from E. coli. Nature *226*, 1214.

Moser, B.A., Chang, Y.T., Kosti, J., and Nakamura, T.M. (2011). Tel1ATM and Rad3ATR kinases promote Ccq1-Est1 interaction to maintain telomeres in fission yeast. Nat. Struct. Mol. Biol. *18*, 1408–1413.

Nakamura, T.M., Morin, G.B., Chapman, K.B., Weinrich, S.L., Andrews, W.H., Lingner, J., Harley, C.B., and Cech, T.R. (1997). Telomerase catalytic subunit homologs from fission yeast and human. Science *277*, 955–959.

Nandakumar, J., and Cech, T.R. (2012). DNA-induced dimerization of the single-stranded DNA binding telomeric protein Pot1 from Schizosaccharomyces pombe. Nucleic Acids Res. *40*, 235–244.

O'Connor, M.S., Safari, A., Xin, H., Liu, D., and Songyang, Z. (2006). A critical role for TPP1 and TIN2 interaction in high-order telomeric complex assembly. Proc. Natl. Acad. Sci. USA *103*, 11874–11879.

Palm, W., and de Lange, T. (2008). How shelterin protects mammalian telomeres. Annu. Rev. Genet. *42*, 301–334.

Pan, L., Hildebrand, K., Stutz, C., Thomä, N., and Baumann, P. (2015). Minishelterins separate telomere length regulation and end protection in fission yeast. Genes Dev. *29*, 1164–1174.

Pettersen, E.F., Goddard, T.D., Huang, C.C., Couch, G.S., Greenblatt, D.M., Meng, E.C., and Ferrin, T.E. (2004). UCSF Chimera–a visualization system for exploratory research and analysis. J. Comput. Chem. *25*, 1605–1612.

Ramsey, K.M., Dembinski, H.E., Chen, W., Ricci, C.G., and Komives, E.A. (2017). DNA and IκBα both induce long-range conformational changes in NFκB. J. Mol. Biol. *429*, 999–1008.

Sato, M., Dhut, S., and Toda, T. (2005). New drug-resistant cassettes for gene disruption and epitope tagging in Schizosaccharomyces pombe. Yeast *22*, 583–591.

Scott, H., Kim, J.K., Yu, C., Huang, L., Qiao, F., and Taylor, D.J. (2017). Spatial organization and molecular interactions of the Schizosaccharomyces pombe Ccq1-Tpz1-Poz1 shelterin complex. J. Mol. Biol. *429*, 2863–2872.

Shay, J.W., and Wright, W.E. (1996). Telomerase activity in human cancer. Curr. Opin. Oncol. *8*, 66–71.

Shay, J.W., and Wright, W.E. (2010). Telomeres and telomerase in normal and cancer stem cells. FEBS Lett. *584*, 3819–3825.

Takai, K.K., Kibe, T., Donigian, J.R., Frescas, D., and de Lange, T. (2011). Telomere protection by TPP1/POT1 requires tethering to TIN2. Mol. Cell *44*, 647–659.

Talkington, M.W., Siuzdak, G., and Williamson, J.R. (2005). An assembly landscape for the 30S ribosomal subunit. Nature *438*, 628–632.

Tefferi, A., Lasho, T.L., Begna, K.H., Patnaik, M.M., Zblewski, D.L., Finke, C.M., Laborde, R.R., Wassie, E., Schimek, L., Hanson, C.A., et al. (2015). A pilot study of the telomerase inhibitor imetelstat for myelofibrosis. N. Engl. J. Med. *373*, 908–919.

Teixeira, M.T., Arneric, M., Sperisen, P., and Lingner, J. (2004). Telomere length homeostasis is achieved via a switch between telomerase- extendible and -nonextendible states. Cell *117*, 323–335.

Wales, T.E., Fadgen, K.E., Gerhardt, G.C., and Engen, J.R. (2008). High-speed and high-resolution UPLC separation at zero degrees Celsius. Anal. Chem. *80*, 6815–6820.

Webb, C.J., and Zakian, V.A. (2012). Schizosaccharomyces pombe Ccq1 and TER1 bind the 14-3-3-like domain of Est1, which promotes and stabilizes telomerase-telomere association. Genes Dev. *26*, 82–91.

Williamson, J.R. (2008). Cooperativity in macromolecular assembly. Nat. Chem. Biol. *4*, 458–465.

Winn, M.D., Ballard, C.C., Cowtan, K.D., Dodson, E.J., Emsley, P., Evans, P.R., Keegan, R.M., Krissinel, E.B., Leslie, A.G., McCoy, A., et al. (2011). Overview of the CCP4 suite and current developments. Acta Crystallogr. D Biol. Crystallogr. *67*, 235–242.

Wu, R.A., Upton, H.E., Vogan, J.M., and Collins, K. (2017). Telomerase mechanism of telomere synthesis. Annu. Rev. Biochem. *86*, 439–460.

Yamazaki, H., Tarumoto, Y., and Ishikawa, F. (2012). Tel1(ATM) and Rad3(ATR) phosphorylate the telomere protein Ccq1 to recruit telomerase and elongate telomeres in fission yeast. Genes Dev. *26*, 241–246.

Zhao, B., Shu, C., Gao, X., Sankaran, B., Du, F., Shelton, C.L., Herr, A.B., Ji, J.Y., and Li, P. (2016). Structural basis for concerted recruitment and activation of IRF-3 by innate immune adaptor proteins. Proc. Natl. Acad. Sci. USA *113*, E3403–E3412.

STAR★METHODS

KEY RESOURCES TABLE

REAGENT or RESOURCE	SOURCE	IDENTIFIER
Antibodies		
Anti-Myc	Sigma-Aldrich	C3956-.2MG
Anti-Flag	Sigma-Aldrich	A8592-.2MG
Anti-Cdc2	Abcam	ab5467
Anti-Ccq1	Hu et al., 2016	N/A
Anti-Rap1	This study	N/A
Anti-Taz1	Gift from Julia Cooper	N/A
Bacterial and Virus Strains		
E. coli XL10-Gold Competent Cells	STRATAGENE	200314
E. coli Rosetta (DE3)	Novagen	70954-3
E. coli BL21(DE3)	NEB	C2527I
List of *S. pombe* Strains used in this study	This study	See Table S2
Chemicals, Peptides, and Recombinant Proteins		
Ni-NTA	QIAGEN	30450
Glutathione HiCap Matrix	QIAGEN	30930
Biotin	OXchem	AX8021635-10 g
Potassium citrate tribasic monohydrate	Sigma-Aldrich	C8385-1KG
Poly(ethylene glycol) 3350	Sigma-Aldrich	88276-1KG-F
cOmplete proteinase inhibitor	Roche	05056489001
Anti-Flag M2 affinity gel	Sigma-Aldrich	A4596
Biocytin	Sigma-Aldrich	B4261-250MG
Magnesium Chloride	BDH	BDH4172-500G
BSA	RPI	A30075-100.0
N+ Membranes	GE Healthcare Amersham Hybond	45 000 927
Deposited Data		
Atomic coordinates and structure factors	This study	PDB: 5WE0, 5WE1, and 5WE2
Raw image Data	This study	https://doi.org/ 10.17632/kjg5pkmkzr.1
Oligonucleotides		
List of oligonucleotides used in this study	This study	See Table S1
Recombinant DNA		
pET28a	Novagen	69864-3
pET28a-His-smt3	Thermo Fisher Scientific	K30001
pGEX-6p-3C	GE Healthcare	28-9546-50
pBirAcm	Zhao et al., 2016	N/A
pET28a-Avi-His-smt3	Zhao et al., 2016	N/A
pFA6a-13Myc-KanMX6	Bähler et al., 1998	N/A
pFA6a-13Myc-hphMX6	Sato et al., 2005	N/A
Software and Algorithms		
Mosflm	N/A	http://www.mrc-lmb.cam.ac.uk/harry/imosflm/ver721/introduction.html
Ccp4	(Winn et al., 2011)	http://www.ccp4.ac.uk/index.php
Coot	(Emsley et al., 2010)	https://www2.mrc-lmb.cam.ac.uk/personal/pemsley/coot/

(*Continued on next page*)

Continued

REAGENT or RESOURCE	SOURCE	IDENTIFIER
PHENIX	(Adams et al., 2010; Afonine et al., 2012)	http://www.phenix-online.org/
CHIMERA	(Pettersen et al., 2004)	https://www.cgl.ucsf.edu/chimera/
Pymol	N/A	https://pymol.org/2/

CONTACT FOR REAGENT AND RESOURCE SHARING

Further information and requests for resources and reagents should be directed to and will be fulfilled by the Lead Contact, Feng Qiao (qiao@uci.edu).

EXPERIMENTAL MODEL AND SUBJECT DETAILS

E. coli Rosetta (DE3) and BL21(DE3)

For protein expression, *E. coli* Rosetta (DE3) [or BL21 (DE3)] was grown in LB at 37°C in a shaker incubator at 220 rpm until an $OD_{600\ nm}$ of between 0.3 and 0.4 was reached after LB was transferred into cold room for 30 min (cold shock). And then the target protein was induced by addition of isopropyl-1-thio-β-$_D$-galactopyranoside (IPTG) to a final concentration of 0.2 mM (16°C) or 0.4 mM (30°C). Expression took place at 16°C for 16 hr or at 30°C for 5 hr.

E. coli XL10-Gold

For cloning, XL10-Gold competent cells were transformed according to the manual provided by the manufacturer and grown on LB agar plates at 37°C overnight.

S. pombe

For *in vivo* assay, the indicated mutants are transformed together with epitope tag and selection marker. The strains are then subjected to Telomere length analysis, Co-IP and ChIP assay.

METHOD DETAILS

Protein expression and purification

Plasmids containing designed protein constructs, either wild-type or mutant, were transformed into Rosetta-BL21 (DE3) cells. IPTG was added to log-phase cell culture to induce protein expression. For *S. pombe* proteins, 0.4 mM IPTG was used and the proteins were expressed for 5 h at 30°C. For *H. sapiens* proteins, 0.2 mM IPTG was used and the proteins were expressed overnight at 16°C. Cells were harvested at 5000 rpm for 10 min and disrupted by sonication in lysis buffer (25mM Tris-HCl at pH 8.0, 350 mM NaCl, 15 mM imidazole, 5 mM β-mercaptoethanol, 1 mM PMSF, 2 mM benzamidine). The supernatant was incubated with Ni-NTA (QIAGEN) resin for 1 h. After washing, the bound protein was eluted from the beads with elution buffer containing 300 mM imidazole. Eluted proteins were then cleaved to remove the tag and further purified by ion exchange and/or gel filtration chromatography.

For various versions of Tpz1-Poz1-Rap1 complex used for crystallization, Tpz1 and Poz1 were cloned into a modified pET28 vector with 6His-SUMO-tag at the N terminus of Poz1. After induction for 5 hours with 0.4 mM IPTG at 30°C, cell was harvested by centrifugation at 4,420 x g. The pellet was mixed with that of 6His-SUMO-tagged Rap1 in lysis buffer [25 mM Tris-HCl pH 8.0, 350 mM NaCl, 15 mM imidazole, 4 mM Benzamidine, 1 mM PMSF, 2 mM β-mercaptoethanol] to sonicate. After lysis, the cell debris was removed by centrifugation at 31,000 g. The supernatant was passed through Ni-NTA agarose (QIAGEN) and eluted with 300 mM imidazole, and then Ulp1 protease was added to remove the 6His-SUMO-tag. The complex was further purified by gel-filtration chromatography Superdex200 equilibrated with 25 mM Tris-HCl pH 8.0, 350 mM NaCl. The purified protein was concentrated to around 10-15 mg/ml and stored at −80°C.

For biotinylated proteins, all target proteins were subcloned into a modified pET28a vector containing the Avi-6His-SUMO tag (Zhao et al., 2016). The biotinylated Avi-6his-SUMO-proteins were expressed in Rosetta BL21(DE3), which were co-transformed with the modified pET28a vector (Kanamycin) and the pBirAcm vector containing the BirA gene (Chloramphenicol). Protein expression was induced with 0.4 mM IPTG in presence of 50uM biotin (Oxchem) at 16°C overnight. The expressed proteins were first purified using Ni-NTA column and further purified using Superdex75, eluted with 20 mM Tris-HCl pH 8.0, 350 mM NaCl.

Crystallization, data collection and structure determination

Initially, crystals of Tpz1$^{475-508}$-Poz1-Rap1$^{470-494}$ complex were grown by hanging drop vapor diffusion at 18°C, with 15∼20% PEG-3350 and 0.175-0.225 M potassium citrate tribasic monohydrate, pH8.3 in the well. To improve the crystal quality, additive screen was carried out. The best crystals were produced with 16%–17% PEG-3350, 0.2-0.25 M potassium citrate tribasic monohydrate

pH 8.3, with 3% 1,5-Diaminopentane dihydrochloride as an additive. The crystals were stepwise transferred into dehydration solutions with 5% increase of PEG-3350 for each step, up to 35% for 3-8 hr. Dehydrated crystals were then gradually transferred into cryo-protectant solution containing additional 18% glycerol and flash-frozen in liquid nitrogen for data collection under 100K. Diffraction date was collected to 2.5 Å resolution at the ALS beamline 501 and processed using Mosflm (Battye et al., 2011). The crystals belong to space group $P2_12_12_1$ with unit cell parameters of a = 83.36, b = 95.39, c = 109.17 and $\alpha = \beta = \gamma = 90^\circ$. Each asymmetric unit contains a dimer of the Tpz1$^{475\text{-}508}$-Poz1-Rap1$^{470\text{-}494}$ complex. Unfortunately, the Se-Met version of Tpz1$^{475\text{-}508}$-Poz1-Rap1$^{470\text{-}494}$ is rather insoluble. To overcome this difficulty, we mutated some Met residues in Poz1 to other hydrophobic residues and obtained Se-Met derivative crystals of Tpz1$^{475\text{-}508}$-Poz1^{3M}-Rap1$^{470\text{-}494}$ (Poz1^{3M}: M26A, M57L, M62A, M114I, M182A and M243A, with only three Met residues left) in a similar condition to the native Tpz1$^{475\text{-}508}$-Poz1-Rap1$^{470\text{-}494}$ complex. These Se-Met derivative crystals belong to space group $P3_121$ with unit cell parameters of a = b = 108.59, c = 132.59; $\alpha = \beta = 90^\circ$, $\gamma = 120^\circ$. Diffraction data were collected to 3.5 Å resolution at the ALS beamline 821 and processed using Mosflm (Battye et al., 2011). With these Se-Met crystals, we obtained initial phases and initial electron density map using program Phenix (Afonine et al., 2012). We then built a partial model for Tpz1$^{475\text{-}508}$-Poz1^{3M}-Rap1$^{470\text{-}494}$ with mainly backbone traced using Coot (Emsley et al., 2010). The model was then used as a template for the molecular replacement program to search against the native dataset of Tpz1$^{475\text{-}508}$-Poz1-Rap1$^{470\text{-}494}$ crystals. The final model for native Tpz1$^{475\text{-}508}$-Poz1-Rap1$^{470\text{-}494}$ was built and refined using Coot (Emsley et al., 2010) and Phenix (Afonine et al., 2012), respectively (PDB: 5WE2). While most regions of Tpz1 and Poz1 are unambiguously assigned in the model, only 3 to 4 residues of Rap1 were identified in the electron density map. In addition, two flexible loops, spanning residues 73-86 and 117-126, were identified in Poz1 with no clear electron density.

In order to achieve a higher resolution of the overall structure and obtain distinct electron density map for Rap1, we replaced those two flexible regions with shorter linker sequences (Poz1 73-86 and 117-126 with GGA and GGGSA, respectively) and fused the N terminus of Rap1 to the C terminus to Poz1 with a linker sequence G.

Crystals from the improved construct, Tpz1$^{475\text{-}508}$-Poz1-Rap1$^{467\text{-}496}$, grew and were handled with the same procedure as described above for the native Tpz1$^{475\text{-}508}$-Poz1-Rap1$^{470\text{-}494}$ complex except for using 1,5-Diaminopentane dihydrochlorideadditive as an additive. The crystals diffracted to 2.3 Å at the ALS beamline 821 and belong to space group P_1 with unit cell parameters of a = 56.72, b = 82.01, c = 103.51 and $\alpha = 89.99^\circ$, $\beta = 89.98^\circ$, $\gamma = 73.96^\circ$. The data was processed using Mosflm (Battye et al., 2011). Each asymmetric unit contains 4 molecules of Tpz1-Poz1-Rap1 complex. The native model of Tpz1$^{475\text{-}508}$-Poz1-Rap1$^{470\text{-}494}$ complex (PDB: 5WE2) was used as a template for molecular replacement. With the high-confidence solution, the final model with clear Rap1 density (for residues 468-484) was further built and refined (PDB: 5WE0).

To solve the structure of Tpz1-Poz1*ΔN* complex, crystals of Tpz1$^{475\text{-}508}$-Poz1$^{29\text{-}249}$ (loop 73-86 in Poz1 was replaced with GGA) were grown under the condition of 3.5%–4.5% reagent alcohol, 0.2-0.3 M magnesium chloride, and 0.1 M Tris-HCl pH 8.0. Diffraction data were collected to 3.2 Å resolution at the ALS beamline 501 and processed using Mosflm (Battye et al., 2011). The crystals belong to space group $P3_1$ with unit cell parameters of a = b = 66.11, c = 123.16 and $\alpha = \beta = 90^\circ$, $\gamma = 120^\circ$. The crystal structure was determined by molecular replacement using the structure of Tpz1$^{475\text{-}508}$-Poz1-Rap1$^{470\text{-}494}$ (PDB: 5WE0) as a template. All structure figures were generated by using program PyMol (http://pymol.sourceforge.net), and the movie was generated by Chimera (Pettersen et al., 2004). Final statistics of data collection and refinement for the structures are shown in Table 1.

Yeast Strains, Gene Tagging, and Mutagenesis

Fission yeast strains used in this study are listed in Table S2. Single mutant strains were constructed by one-step gene replacement of the entire ORF with the selectable marker. Double and triple mutant strains were produced by mating, sporulation, dissection, and selection followed by PCR verification of genotypes. Genes were fused to specific epitope-tags at the C terminus by homologous recombination; the pFA6a plasmid modules were used as templates for PCR (Bähler et al., 1998; Sato et al., 2005). Point mutations were made by site-directed mutagenesis PCR using the high fidelity polymerase *Pfu* (Agilent). All mutations were confirmed by DNA sequencing (Eton, San Diego, CA).

GST-pulldown assay

GST-pulldown assays were performed as previously described. Briefly, 15 μg GST fusion protein was incubated with 20 μL glutathione Sepharose resin (QIAGEN) in 30 μL GST pulldown buffer [50 mM Tris-HCl at pH 8.0, 200 mM NaCl, 10mM β-ME, 0.1% Tween-20]. Then the resin was washed and incubated with the target protein (20 μg in 120 μL GST pulldown buffer) for 1 h. The bound proteins were resolved by 10% SDS-PAGE and visualized by Coomassie blue staining.

Telomere Length Analysis

The telomere length of each strain was analyzed as previously described (Liu et al., 2015). Briefly, genomic DNA was prepared from 5 mL liquid culture in YEAU. For all strains, the telomeric fragments were released by EcoRI (NEB) digestion and separated on 1% agarose gels. Southern blots with both telomeric and *pol1*$^+$ probe were visualized using Typhoon scanner (GE Healthcare).

Co-Immunoprecipitation

Cells were cultured in 50 mL YEAU and harvested till log phase. Cell pellets were cryogenically disrupted with FastPrep MP with two pulses (60 s) of bead-beating in ice-cold lysis buffer [50 mM HEPES at pH 7.5, 140 mM NaCl, 15 mM EGTA, 15 mM $MgCl_2$,

0.1% NP40, 0.5 mM Na_3VO_4, 1 U/ml DNase, 1 mM NaF, 2 mM PMSF, 2 mM benzamidine, Complete proteinase inhibitor (Roche)]. Whole cell extract was cleared by centrifugation twice, 10 min each. Then, the concentration of the supernatant was measured using Bradford protein assay (Bio-Rad) and was adjusted to 12 mg/ml with lysis buffer. 300 μL cell extracts were incubated with anti-Flag M2 affinity gel (Sigma), anti-Myc (9E10 from Santa Cruz Biotechnology) or anti-Ccq1 rabbit serum or anti-Rap1 rabbit serum plus IgG beads (Roche) for 2 h at 4°C. The proteins were eluted with 30 μL 0.1 M glycine (pH2.0) at room temperature for 10 min with gentle shaking followed by Tris-HCl (pH8.0) neutralization. Eluted proteins were resolved by 8% SDS-PAGE and then subjected to Western Blotting. Western blot analysis was performed using monoclonal anti-Flag (M2-F1804, from Sigma), monoclonal anti-Myc (from Covance), anti-Ccq1 rabbit serum (Hu et al., 2016), anti-Rap1 rabbit serum, or anti-Cdc2 (y100.4, from Abcam).

Isothermal Calorimetry (ITC)

All ITC experiments were carried out in buffer B350 (25 mM Tris-HCl pH 8.0, 350 mM NaCl, and 0.5 mM TCEP) using a MicroCal iTC 200 (Malvern Instruments, Malvern UK) at 25°C. Data were analyzed using Origin 7.0 (OriginLab, Northhampton, MA) software.

Biolayer Interferometry (BLI) and K_d Calculation

BLI were performed in black 96-well plates (Greinerbio-one, Germany) on Octet^{RED}96 instrument (ForteBio, USA). Prior to use, biosensors were soaked in binding assay (BA) buffer (20 mM Tris-HCl, pH 8.0, 350 mM NaCl, 0.2% NP-40, 0.5 mM DTT, 0.1% BSA) for at least 10 min. BLI assays consisted of six steps, all performed in BA buffer: initial base line (30 s), loading (120 s), Quenching (120 s), base line (60 s), association (30 s) and dissociation (90 s). Each biotinylated protein was immobilized on each Streptavidin biosensor tip. For the loading step, protein concentrations were adjusted to yield signal intensity in the range of 2 to 3 nm. To quench free streptavidin, 4 μg/ml of biotin analog, biocytin (Sigma), was used in BA buffer. Biotinylated protein-loaded sensors itself was measured as a control to subtract from experimental values before data processing. Sensorgrams were fit using global/1:1 binding model by ForteBio Data analysis version 9.0, from which the equilibrium dissociation constant (K_d) and association (k_{on}) and dissociation (k_{off}) rate constants were calculated.

Size-Exclusion Chromatograph-Multi-Angle Light Scattering (SEC-MALS)

SEC-MALS experiments were performed at 30°C with a P2500 and P3000 silica-based columns and Viskotek GPCmax/RI/DLS/MALS detection system (Malvern Instruments, Malvern, UK). Columns were equilibrated with buffer containing 25 mM Tris-HCl pH 8.0, 350 mM NaCl), followed by analytical grade bovine serum albumin (BSA) (Sigma-Aldrich, St. Louis, Mo.) injection for detector calibration and reference. All three protein complexes, the constructs used for solving the crystal structures, were injected into the same column for molar mass determination, respectively. The flow rate during experimental was maintained at 1 ml/min, with 100 μL injection volumes per trial.

Hydrogen/deuterium exchange mass spectrometry (HXMS)

HXMS was performed using a Waters Synapt G2Si equipped with nanoACQUITY UPLC system with H/DX technology and a LEAP autosampler essentially as described previously (Ramsey et al., 2017). The final concentrations of proteins and complexes in each sample were 5 μM. For each deuteration time, 4 μL complex was equilibrated to 25°C for 5 min and then mixed with 56 μL D_2O buffer (25mM Tris-HCl at pH 8.0, 350 mM NaCl, 15 mM imidazole, 0.5 mM TCEP) for 0, 0.5, 1, 2, or 5 min. The exchange was quenched with an equal volume of quench solution (3 M guanidine, 0.1% formic acid, pH 2.66).

The quenched sample was injected into the 50 μL sample loop, followed by digestion on an in-line pepsin column (immobilized pepsin, Pierce) at 15°C. The resulting peptides were captured on a BEH C18 Vanguard pre-column, separated by analytical chromatography (Acquity UPLC BEH C18, 1.7 μM, 1.0 X 50 mm, Waters Corporation) using a 7%–85% acetonitrile in 0.1% formic acid over 7.5 min, and electrosprayed into the Waters SYNAPT G2Si quadrupole time-of-flight mass spectrometer. The mass spectrometer was set to collect data in the Mobility, ESI+ mode; mass acquisition range of 200–2,000 (m/z); scan time 0.4 s. Continuous lock mass correction was accomplished with infusion of leu-enkephalin (m/z = 556.277) every 30 s (mass accuracy of 1 ppm for calibration standard). For peptide identification, the mass spectrometer was set to collect data in MS^E, ESI+ mode instead.

The peptides were identified from triplicate MS^E analyses of 10 μM protein, and data were analyzed using PLGS 2.5 (Waters Corporation). Peptide masses were identified using a minimum number of 250 ion counts for low energy peptides and 50 ion counts for their fragment ions. The peptides identified in PLGS were then analyzed in DynamX 3.0 (Waters Corporation). The following cut-offs were used to filter peptide sequence matches: minimum products per amino acid of 0.2, minimum score of 7, maximum MH+ error of 5 ppm, a retention time standard deviation of 5%, and the peptides were present in two of the three ID runs. After back-exchange correction (~30%), the relative deuterium uptake for each peptide was calculated by comparing the centroids of the mass envelopes of the deuterated samples with the undeuterated controls following previously published methods (Wales et al., 2008). The experiments were performed in triplicate, and independent replicates of the triplicate experiment were performed to verify the results. The back-exchange corrected data were plotted in Kaleidagraph and fitted with a double exponential curve.

QUANTIFICATION AND STATISTICAL ANALYSIS

All ChIP assay were performed on three independent experiments. The Southern blot data of ChIP assay were quantified using ImageQuantTL software, which were further plotted and fit using GraphPad Prism 5. All ITC and BLI experiments were repeated twice and representative results were shown. For hydrogen/deuterium exchange experiments, three independent reactions were performed and the deuterium uptake values were averaged. The error bars represent the standard deviation. Occasionally, the errors are very small (they are within the symbols), because the experiments were carried out by a liquid-handling robot.

DATA AND SOFTWARE AVAILABILITY

The atomic coordinates and structure factors reported in this paper have been deposited in the Protein Data Bank (PDB). The accession numbers for the structures reported in this paper are PDB: 5WE0, 5WE1, and 5WE2. The unprocessed image files used to prepare the figures in this manuscript have been deposited to Mendeley Data and are available at https://doi.org/ 10.17632/kjg5pkmkzr.1.